Water Resources Research

RESEARCH ARTICLE
10.1029/2024WR037509

The Influence of Horizontal Dispersion on Residence Times in Shallow Lakes

Eiji Masunaga[1], **Oliver B. Fringer**[2], **Tatsumi Kitamura**[3], **and Takao Ouchi**[3]

[1]Global and Local Environment Co-creation Institute, Ibaraki University, Ibaraki, Japan, [2]The Bob and Norma Street Environmental Fluid Mechanics Laboratory, Department of Civil and Environmental Engineering and Department of Oceans, Stanford University, Stanford, CA, USA, [3]Ibaraki Kasumigaura Environmental Science Center, Ibaraki, Japan

Key Points:

- Circulation in lakes is investigated with numerical simulations
- Shape of lakes largely influences tracer dispersions
- The water residence time increases as dispersion increases owing to the scale of the lake

Correspondence to:

E. Masunaga,
eiji.masunaga.office@vc.ibaraki.ac.jp

Citation:

Masunaga, E., Fringer, O. B., Kitamura, T., & Ouchi, T. (2025). The influence of horizontal dispersion on residence times in shallow lakes. *Water Resources Research*, *61*, e2024WR037509. https://doi.org/10.1029/2024WR037509

Received 13 MAR 2024
Accepted 24 JAN 2025

Author Contributions:

Conceptualization: Eiji Masunaga
Data curation: Eiji Masunaga, Tatsumi Kitamura, Takao Ouchi
Formal analysis: Eiji Masunaga
Investigation: Eiji Masunaga, Tatsumi Kitamura, Takao Ouchi
Methodology: Eiji Masunaga, Oliver B. Fringer
Project administration: Eiji Masunaga
Writing – original draft: Eiji Masunaga, Oliver B. Fringer
Writing – review & editing: Eiji Masunaga, Oliver B. Fringer, Tatsumi Kitamura, Takao Ouchi

Abstract This study presents results of circulation and residence time in lakes influenced by wind-induced mixing investigated with numerical simulations. The study area is Lake Kasumigaura, a continuous lake system primally consisting of two lakes, West Lake and North Lake. Although metrological conditions and depths are similar for both lakes, the surface area and shape of the lakes are very different. A numerical model resolves the primary features of the wind-driven circulation in the lake system and is forced by observed river discharges and wind stress. A passive tracer released from the river mouths is used to estimate the residence time and evaluate mixing processes. Wind-driven flow dominates the kinetic energy in the lakes and induces chaotic motions leading to tracer dispersion which is largely influenced by the shape of the lakes. Results indicate that the residence time is much longer in the well-mixed middle basin of West Lake than North Lake. The estimated horizontal tracer diffusivity is approximately three times larger for the large West Lake than for the small-narrow North Lake. This study suggests that the surface area and shape of lakes in which the flow is predominantly wind driven largely influences circulation, water exchange processes and residence times in lakes.

1. Introduction

It is well known that water residence times play an important role in eutrophication, primary production and plankton growth rates in lakes (e.g., Busu & Pick, 1996; Romo et al., 2013; Vollenweider, 1976). Generally speaking, under favorable conditions with sufficient nutrient and light availability, primary production increases as the residence time increases because phytoplankton are subject to favorable growth conditions for longer times. Field observations conducted by Busu and Pick (1996) showed that phytoplankton and zooplankton biomass increase with increase in residence times in a lake. These studies imply that the residence time is an important factor to understand ecosystem and eutrophication in lakes and reservoirs. Despite its importance, details of how circulation and associated dispersion and mixing processes affect the residence time in lakes are not well understood.

A common approach to estimate transport and residence times is to use chemical properties obtained in situ. Dye-tracer experiments, such as using rhodamine WT-20, have been conducted to estimate transport in rivers, lakes and oceans (e.g., Grimes et al., 2020; Kratzer & Biagtan, 1997; Morillo et al., 2006). Kratzer and Biagtan (1997) estimated transport time scales in a river from dye release experiments. Grimes et al. (2020) observed the dye concentration by making use of an aerial remote sensing technique and revealed detailed structures of dye released from the coast. Stevens et al. (2004) conducted dye tracer experiments in a shallow lake showing enhanced diffusive events caused by wind-driven shear dispersion and internal waves. They also found that tracer diffusivity increases as the horizontal length scale increases, which can explained with the well-known diffusion diagram suggested by Okubo (1971). Chemical properties of water, such as alkalinity, heavy metals and mineralization rates, have been also used to estimate water transport in aquatic systems (e.g., Ambrosetti et al., 2003; Eshleman & Hemond, 1988; Monsen et al., 2002). Monismith et al. (2002) estimated the horizontal shear dispersion coefficient in a brackish estuary using observed horizontal salinity distributions and river flows. However, due to difficulties in observing water properties in the field, a complete picture of water circulation processes in lakes cannot be obtained with in situ field observations.

Numerical simulations have been frequently used to investigate circulation and residence times in lakes (e.g., Auger et al., 2024; Dargahi & Setegn, 2011; Li et al., 2011). Li et al. (2011) conducted numerical simulations of a large lake and reported that the residence time is largely influence by wind stress. Numerical simulations by

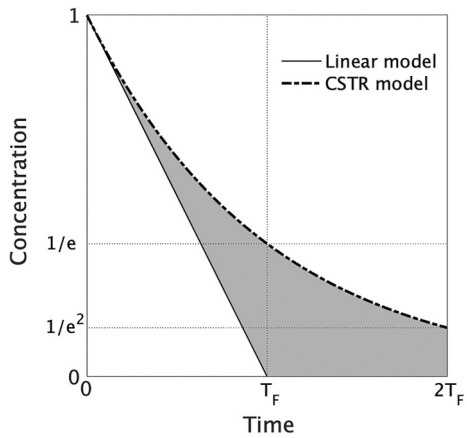

Figure 1. The domain-averaged tracer concentration from the linear model (solid line) and continuously stirred tank reactor model (dash-dotted line).

Dargahi and Setegn (2011) also showed that water circulations and mass transport in a lake are primally explained by wind forcing. They estimated a flushing time of 19 months based on numerical results. Rueda et al. (2006) reported that the residence time is sensitive to mixing and transport conditions modified over seasonal to diurnal time scales. Lucas et al. (2002) employed a Lagrangian particle tracking model for a tidal delta and showed enhanced mass transport between the delta and connected channels caused by tidal flows. da Silva et al. (2019) conducted numerical simulations for a shallow lagoon and suggested that gyres generated by winds enhance the stagnation of water leading to an increase in the residence time. Rayson et al. (2016) estimated the spatial distribution of the residence time in a shallow estuary using a Lagrangian particle tracking model. They found that the residence time is largely influenced by the changing river discharge and locations. Auger et al. (2024) conducted high-resolution numerical simulations for a lake and suggested that short residence times in small bays in large lakes are important for understanding lake environments.

It is well known that large-scale water circulation is also significantly influenced by the earth's rotation (Coriolis forcing). Wind-induced currents in enclosed lake systems are also affected by the earth's rotation (e.g., Amadori et al., 2020; Ito et al., 2023; Valbuena et al., 2022). Ito et al. (2023) reported that jet-like currents along coastal boundaries due to the geostrophic balance suppress wind-induced upwelling. Valbuena et al. (2022) conducted numerical simulations of a moderate size lake, Lake Tahoe, and they suggested that wind-induced circulation is not simply explained by a single conceptual model related to the earth's rotation.

The residence or flushing time scale in a domain can be simply described as

$$T_f = \frac{V}{Q}, \tag{1}$$

where V is the domain volume and Q is the flow rate of water into or out of the domain. In this case, the total volume in the domain does not change,. viz., the outflow is equal to the inflow. If we assume that the initial tracer concentrations in the domain and inflowing water are C_0 and zero, respectively, and there is no mixing and the outflow concentration is C_0, the domain-averaged tracer concentration linearly decreases with time according to

$$C_{\text{linear}}(t) = C_0(T_f - t)/T_f \quad \text{if } t < T_f, \tag{2}$$

where t is time and the $C_{\text{linear}}(t) = 0$ when $t = T_f$ (Figure 1). In this study, this zero-mixing model is referred as the "linear model." However, in realistic aquatic systems, the inflowing water mixes with the water within the domain. The completely mixed condition gives the continuously stirred tank reactor (CSTR) model for the concentration as

$$C_{\text{CSTR}}(t) = C_0 \exp\left(-t/T_f\right). \tag{3}$$

The concentration is C_0/e at T_f in this model (Figure 1). Monsen et al. (2002) documented details of flushing/residence time scales and reported that the domain-averaged tracer concentration in a tidal delta is well represented by the CSTR model. They also show that the residence time varies spatially and suggested that spatial patterns of the residence time regulates spatial patterns related to biological processes.

In lakes and reservoirs, owing to mixing conditions that lie somewhere between complete and no mixing, the domain-averaged tracer concentration is bounded by the concentrations given by the linear (Equation 2) and CSTR models (Equation 3) (the gray shaded area in Figure 1). This implies that mixing conditions strongly influence the residence time and water exchange processes in closed systems, viz., the residence time increases as mixing increases.

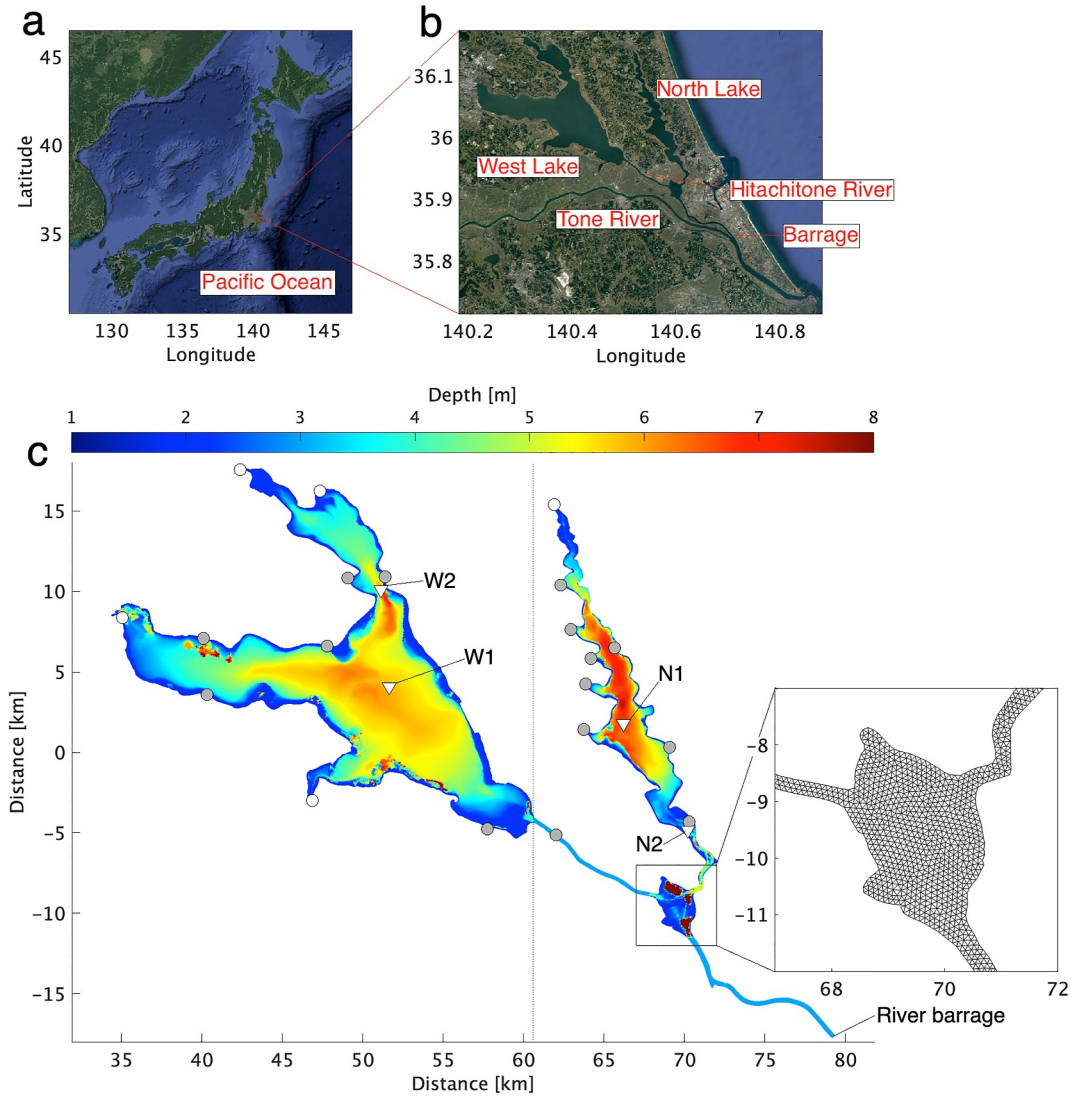

Figure 2. (a, b) Maps of the study area, and (c) bathymetry of the model domain and example of a zoomed-in view of the triangular grid (right sub-panel). Gray triangles in panel (c) show the locations of the moored current measurements (Stn. N1, N2, W1, and W2). White and gray filled circles in panel (c) indicate the location of point source river discharge inputs. Vertical black dotted line in panel (c) represents the boundary between the west and east domains for wind forcing, $x = 61$ km.

As described above, mixing processes directly influence the residence time in lakes and reservoirs. Horizontal mixing/dispersion processes in lakes have been investigated with dye and tracer release experiments (e.g., Choi et al., 2020; Peeters & Hofmann, 2015; Stocker & Imberger, 2003). Stocker and Imberger (2003) conducted drifter experiments in a starfield lake and reported horizontal dispersion associated with internal waves. Drifter experiments by Peeters and Hofmann (2015) showed a robust relationship between horizontal dispersion and time/horizontal scales in a medium-sized lake. Choi et al. (2020) combined dye and drifter experiments and found that lateral shear motions strongly influence horizontal dispersion in a large lake. However, the residence time associated with mixing conditions has not been thoroughly investigated in previous studies. In order to address this issue, we conducted numerical simulations for two shallow lakes in the Lake Kasumigaura continuous system with a passive tracer from rivers to investigate transport, circulation and residence times (Figure 2). The reminder of this paper is structured as follows. Sections 2 describes details of the study site, model configuration and field campaigns. Section 3 presents field observations and model validation. Numerical results and discussion associated with tracer dispersion and residence times are described in Section 4. Finally, Section 5 summarizes this study with the major conclusions.

2. Material and Methods

2.1. Study Area

The study area is Lake Kasumigaura, a continuous lake system, located in Ibaraki Prefecture, the middle of the Japanese mainland (Figure 2). The lake system primarily consists of two lakes, which are referred to as West Lake and North Lake. Although depths of the two lakes are similar in the range of 5–7 m at their deepest, the shapes of the coast lines differ significantly (Figure 2c). Isolated regions deeper than 8 m are created by artificial drilling. North Lake is narrow and its length is approximately 20 km with a surface area of approximately 36 km^2. West Lake is much wider than North Lake and the surface area of West Lake is approximately 172 km^2 with a large middle basin. The two lakes are connected by the Hitachitone River (Figure 2b). The catchment area of Lake Kasumigaura is estimated as 2,157 km^2 and numerous rivers and creeks flow into the upstream lake. The river barrage is located at the downstream end of Lake Kasumigaura and controls water outflows by opening/closing of gates (Figure 2c). The study area is connected to the Pacific Ocean through the Tone River. Originally, Lake Kasumigaura was a brackish-water lagoon due to saline water intrusion. However, construction of the river barrage in 1960s eliminated saline water intrusion, and thus water in the lake is now completely fresh. During normal operation, the gates at the river barrage are closed during high tides to prevent salt water intrusion, while they are open during low tides to release lake water to the Pacific Ocean.

Severe water quality issues have been reported for Lake Kasumigaura. Eutrophication due to human activities has led to harmful algae blooms of Microcystis in summer (Homma et al., 2008). Eutrophication and algae blooms enhance the light extinction coefficient (~1–2 m^{-1}) (Nakamura & Aizaki, 2016), which suppress photosynthesis in the bottom layer resulting in hypoxia (Masunaga et al., 2023). The Ibaraki Prefecture Government has attempted to reduce eutrophication by reducing nitrogen and phosphorus loads into the lake since the 1980s. However, water quality has not improved, making a clear understanding of water circulation and residence times in Lake Kasumigaura is essential for the creation of effective solutions for water quality management.

2.2. Numerical Model Configuration

We employed the hydrodynamic numerical model SUNTANS (Stanford Unstructured Nonhydrostatic Terrain-following Adaptive Navier-Stokes Simulator) (Fringer et al., 2006), to reproduce water circulation in Lake Kasumigaura. Although this model can solve for the nonhydrostatic pressure, we used its hydrostatic version to reduce the computational cost. The hydrostatic approximation is valid method when the ratio of the relevant vertical to horizontal scales is small (Vitousek & Fringer, 2011). Effects of nonhydrostatic pressure are expected to be negligible for basin-scale circulation processes with horizontal extents of O(1–10 km) in our study area with depth of O(1) m. The momentum advection and viscosity terms are discretized in space with second-order accurate, central differencing in SUNTANS. The model domain consists of a triangular grid that resolves the Lake Kasumigaura continuous system with a horizontal grid spacing of approximately 100 m (Figure 2c). The bathymetry is provided by Geospatial Information Authority of Japan (https://www.gsi.go.jp/kankyochiri/lakedata.html). The vertical grid spacing is set at 1 m. The maximum depth is set at 10 m, viz., for a total of ten z layers. The average depth is 4.2 and 4.5 m in the model domains of West Lake and North Lake, respectively. The bottom drag coefficient is set at 2.5×10^{-3}. The Coriolis parameter is specified at 8.6×10^{-5} rad s^{-1} corresponding to a latitude of 36° N. The computational time step is 10 s to satisfy the Courant-Friedrichs-Lewy (CFL) criterion, viz., to maintain numerical stability related to explicit advection of momentum and scalars. The horizontal and vertical viscosities are set to 0.1 and 0.01 m^2 s^{-1}, respectively, based on stability of the central differencing scheme for momentum advection.

Thirty six rivers are considered in the model reported by the Ibaraki Prefecture (Maeda, 2012). River discharges are forced as water inflows at lateral boundaries along the coast. If two or more river mouths are located closely, their discharges are combined into one single discharge. Consequently, the model is forced by 20 river discharge points (see details Appendix A). The annual average river discharge observed in 2008 for all rivers is available (Maeda, 2012). However, continuous observed river discharge records are available only for six rivers from Japanese Ministry of Land, Infrastructure, Transport and Tourism (MLIT, http://www1.river.go.jp/) (indicated by white filled circles in Figure 2c, the number of the white filled circles is five, because some adjoining river mouths are merged). In order to obtain time series of river discharges for all rivers, we define river discharges using the annual averaged discharges reported by the Ibaraki Prefecture report (Maeda, 2012) and the river discharge weight estimated from time series of the observed river discharge records as follows

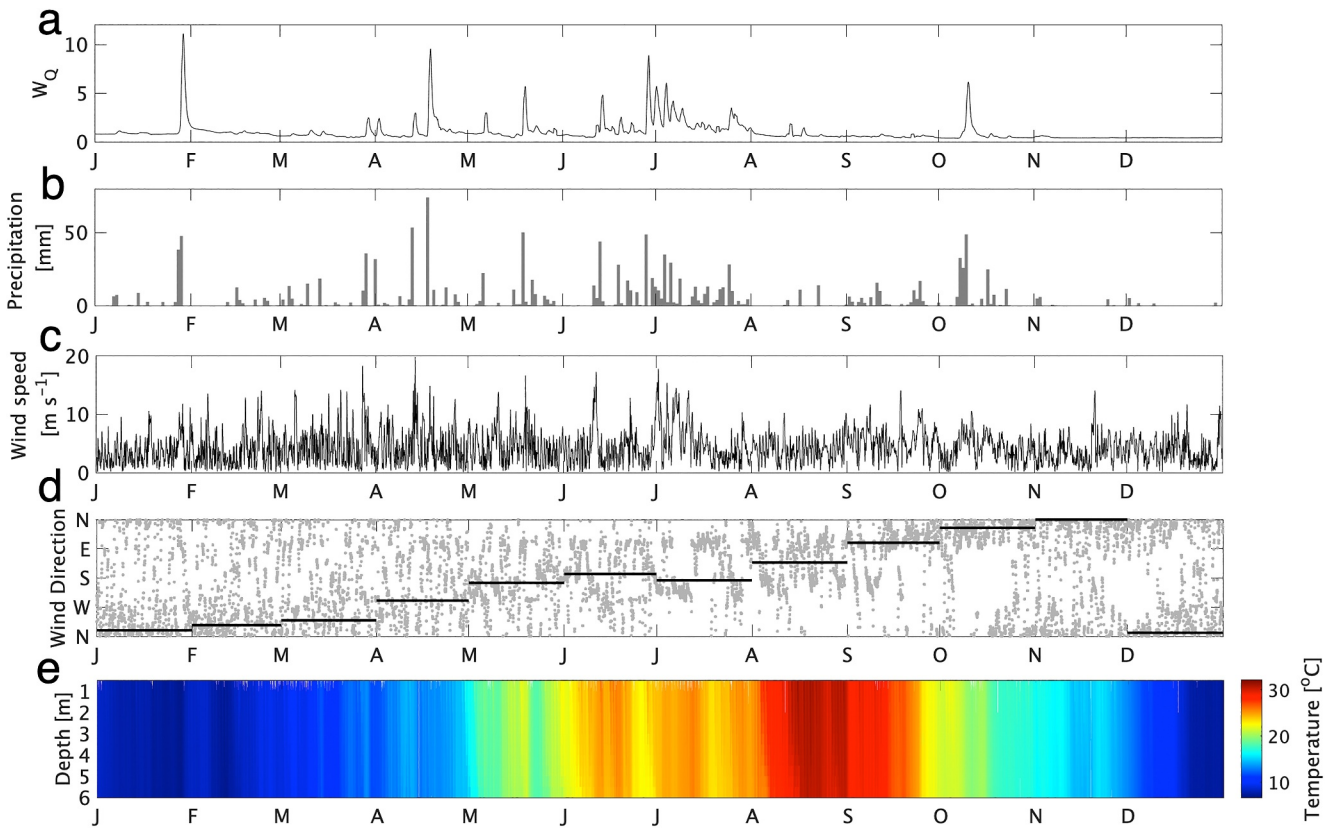

Figure 3. (a) The weight for river discharges, W_Q. (b) daily precipitation over the Lake Kasumigaura catchment, and (c–d) wind forcing data, including (c) wind speed and (d) direction over West Lake. (e) Temperature time series observed at the Kamaya Monitoring Station near Stn. N1 in North Lake.

$$Q_i(t) = W_Q(t)\, Q_{M(i)}, \tag{4}$$

where Q_i is the river discharge for each river, subscript i denotes the number of the river mouth (total of 20 river mouths), W_Q is the weight of the river discharge and Q_M is the annually averaged river discharge from Maeda (2012). Q_M ranges between 0.32 and 12.68 m^3 s^{-1} (see details in Appendix). The weight of the river discharge, W_Q, is obtained from the averaged observed river discharge at the six rivers and is given by

$$W_Q(t) = Q_{\mathrm{ObsM}}(t)/\overline{Q_{\mathrm{ObsM}}}, \tag{5}$$

where Q_{ObsM} is the average river discharge from observations of continuous river discharge records at the six rivers and the overbar is the time average. 24 hours running mean averaged W_Q is used in the model to avoid numerical instability due to short-term extremely high discharges. Time series of W_Q are shown in Figure 3a and appear to be consistent with the precipitation (Figure 3b). The daily precipitation is obtained from the daily averaged precipitation over seven weather stations within the catchment area operated by the Japan Meteorological Agency (JMA, https://www.jma.go.jp/jma/index.html). The maximum and minimum values of W_Q are 11.1 and 0.4, respectively. Boundary velocities at the river mouths are constant in the vertical since the boundaries are shallow, ∼1 m. The downstream boundary at the river barrage is forced by the surface height using continuous observation data obtained from the Japan Water Agency (JWA). The surface height generally decreases (increases) when the water gates at the river barrage are opened (closed) due to water release (river discharge). Changes in the surface height forcing generate barotropic flows at the downstream boundaries due to water inflows/outflows controlled by the river barrage. A benefit of specifying the free-surface height at the downstream boundary is to ensure a constant water volume in the model domain, viz., the river discharges from the upstream boundaries are balanced by outflows at the downstream boundary.

A passive tracer is used to investigate transport and dispersion of water from the rivers. The initial value of the tracer concentration (C) is set at one in the numerical domain and the tracer concentration at the upstream river boundaries is set at zero. The tracer is then transported by pure advection with no explicit diffusion using the flux-limiting scalar transport scheme of Casulli and Zanolli (2005) with the Superbee flux limiter in the SUNTANS model. We rely on numerical diffusion to account for the horizontal mixing under the assumption that unresolved processes will be diffused, or mixed, once the large-scale stirring and dispersion processes, which are well resolved, produce grid-scale motions. This is typical of circulation models which do a reasonable job of modeling the horizontally driven mixing as long as the large-scale processes are resolved (Fringer et al., 2019).

The surface boundaries are forced by observed hourly wind stress approximately 10 m above the water surface at two weather stations operated by JWA. Locations of the weather stations are indicated by W2 and N1 in West Lake and North Lake, respectively, in Figure 2c. The surface wind stress is estimated by $\boldsymbol{\tau}_w = \rho_a C_D \mathbf{U}_\mathbf{w} \cdot |\mathbf{U}_\mathbf{w}|$, where ρ_a is air density (1.2 kg m^{-3}), C_D is the drag coefficient (1.5×10^{-3}) and $\mathbf{U}_\mathbf{w}$ is wind speed vector. The west (east) domain where x-distance less (more) than 61 km is forced by wind stress obtained at Stn. W2 (N1) (Figure 2c). Although wind forcing is separated in the west and east model domains, observed wind speed over the two lakes is nearly the same. The correlation coefficient of wind speeds is 0.82 and the ratio between wind speeds over North Lake and West Lake is 1.02. The wind forcing over West Lake is shown in Figures 3c and 3d. The magnitude of the wind speed varies up to 20 m s^{-1} and its annual average is 4.3 m s^{-1} over West Lake. The wind direction shows a clear seasonal pattern; dominant north and south winds in winter and summer, respectively. This seasonal pattern is caused by seasonal monsoon-trade winds at mid-latitudes. In addition to numerical simulations with the wind forcing, we conducted a model run without wind forcing. The model cases with and without the wind forcing allow us to isolate the effects of winds on water circulation and tracer transport. In addition to these two model runs, we conducted two additional model runs without the earth's rotation (the Coriolis forcing) to evaluate its effects on the lake system. The computational period is from January 1 to 31 December 2020 (total 366 days). The velocity field is initially quiescent throughout the domain.

The water density is 997.0 kg m^{-3} throughout the domain, which corresponds to fresh water with a temperature of 25°C. Temperature at the river discharges is also set at 25°C, and hence density currents due to a difference between the lake and river waters are not considered in the model. It is well known that stratification develops during the summer season in the lakes (e.g., Masunaga et al., 2023). However, strong stratification appears only in the summer season and disappears or weakens at night due to daily sea-breeze and nigh-time surface cooling, because depths of the lakes are shallow, with depths of 5–7 m (Masunaga et al., 2023). Intensified stratification typically appears with durations of one day to 1 week in summer. Indeed, observed temperature time series appear to be vertically uniform over annual time scales (Figure 3e). The flushing time scale is estimated at approximately 6 months for West Lake and is much longer than the durations of daily vertical mixing and temporally intensified stratification in summer. In addition, observed velocity data do not show clear baroclinic vertical flow variations (see Appendix B). Based on these reasons, we assume that short term stratified events in the shallow lakes can be ignored to investigate horizontal tracer dispersion processes. Therefore, this study does not consider surface heat flux and stratification.

3. Field Observations and Model Validation

We conducted field observations using moored acoustic Doppler current profilers (ADCPs; Nortek 2 kHz Aquadopp Profiler) to validate the accuracy of the numerical model. Four ADCPs were deployed at four locations from 17 June to 16 July 2020 (Figure 2c, Stn. N1, N2, W1, and W2). Observed data between June 18–July 16 was used to validate the model results. The ADCPs measured velocity data with a vertical interval of 0.5 m with a burst interval of 10 min. The deepest ADCP bin is located 0.9 m above the lake bed. Each sampled data at every 10 min consists of time-averaged data over 15 pings sampled at 1 Hz, viz., the ADCPs recorded 15-s time averaged data at an interval of 10 min. Hourly and vertically averaged velocity data are compared to model predictions because observed velocities at each layer show high-frequency noisy-like motions (see Appendix B). The free-surface height obtained from the ADCP pressure gauges is also used for model validation.

Comparisons of the surface height and velocity at Stn. N1 in the middle basin of North Lake are plotted in Figure 4. Surface height variations agree with the model (Figure 4a). Short-term surface height variations are induced by water gate operation at the downstream end of Lake Kasumigaura (Figure 4, gray-shaded periods). Modeled water velocities also show a similar pattern as the observed results (Figures 4b and 4c). The velocity

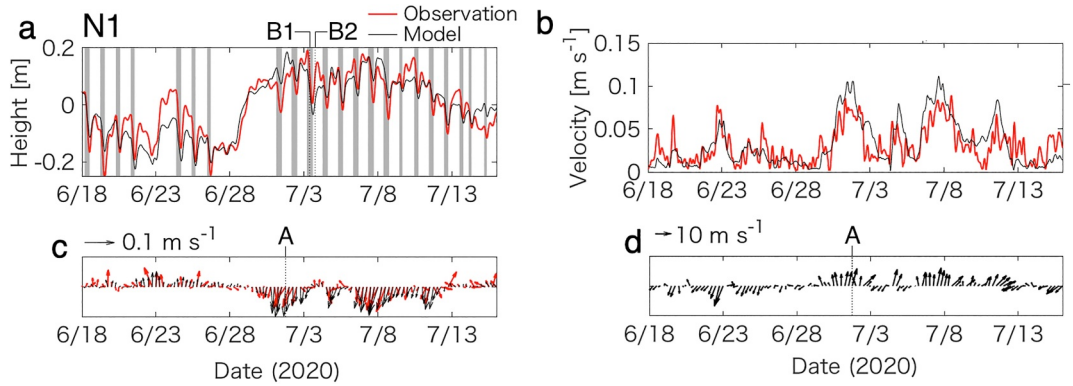

Figure 4. (a–d) Observed and modeled results of (a) surface height, (b) vertically averaged velocity magnitude and (c) velocity vectors of the vertically averaged velocity at Stn. N1, and (d) wind forcing over the North Lake. Periods A, B1, and B2 are referenced in Figures 5 and 6, respectively. Gray-shaded areas in panel (a) indicate durations when the water gates at the rive barrage were opened.

magnitude is enhanced by up to approximately 0.1 m s^{-1} when south (northward) wind blows (Figures 4b and 4d, July 1, period A). Meanwhile, the direction of currents is southward and is opposite to the wind direction in this period (Figure 4c, period A). The opposite directions of wind and currents appears during the entire mooring period, as explained in the following section.

The surface height at Stn. N2 at the downstream end of North Lake shows similar fluctuations as in the lake basin (Figure 5a). However, there are periods in which the predicted surface height disagrees with observations(for example, during June 23–28). These likely result from an inability to resolve details of the surface wind stress which is obtained from just two locations around the lakes. In addition, over/under estimations of the river discharges used in the model would lead to gaps between the observed and modeled free-surface heights. Large velocity fluctuations occur at Stn. N2 with magnitudes of approximately 0.1–0.15 m s^{-1} (Figures 5b and 5c). These fluctuations occur when the water gates at the river barrage open, followed by rapid recovery of the surface height and motions in the opposite direction after they are closed (Figure 5, gray-shaded periods indicate water release or open gate

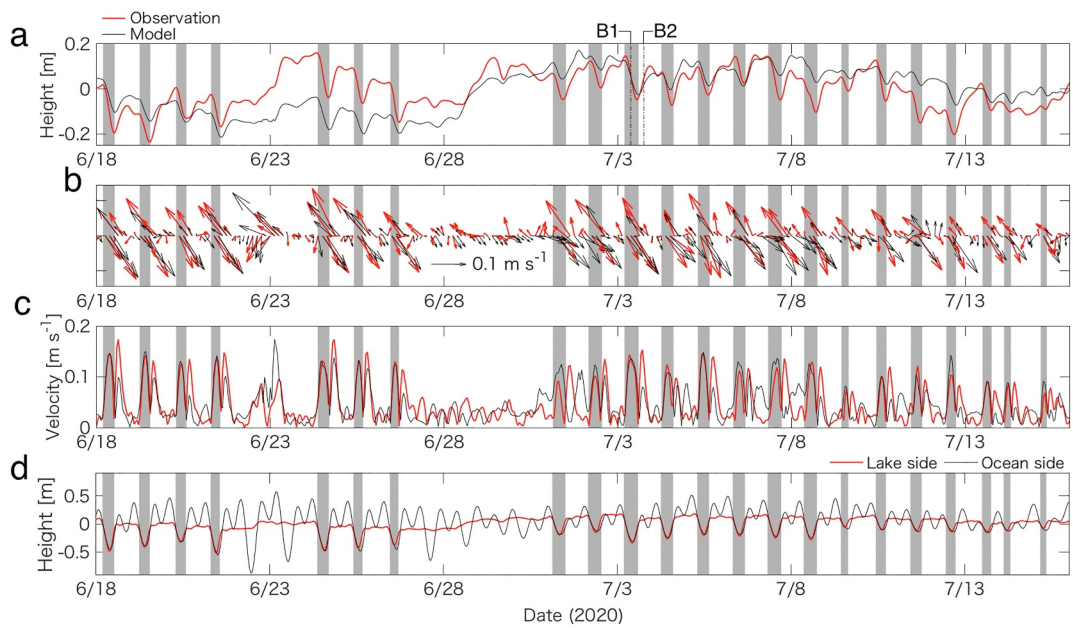

Figure 5. (a–d) Observed and modeled results of (a) surface height, (b) velocity vectors of the vertically averaged velocity, (c) vertically averaged velocity magnitude at Stn. N2, and (d) observed surface height on the lake (red) and ocean (black) sides of the river barrage. The period shown in this figure is the same as in Figure 4, but the horizontal axes are extended for visualization purposes.

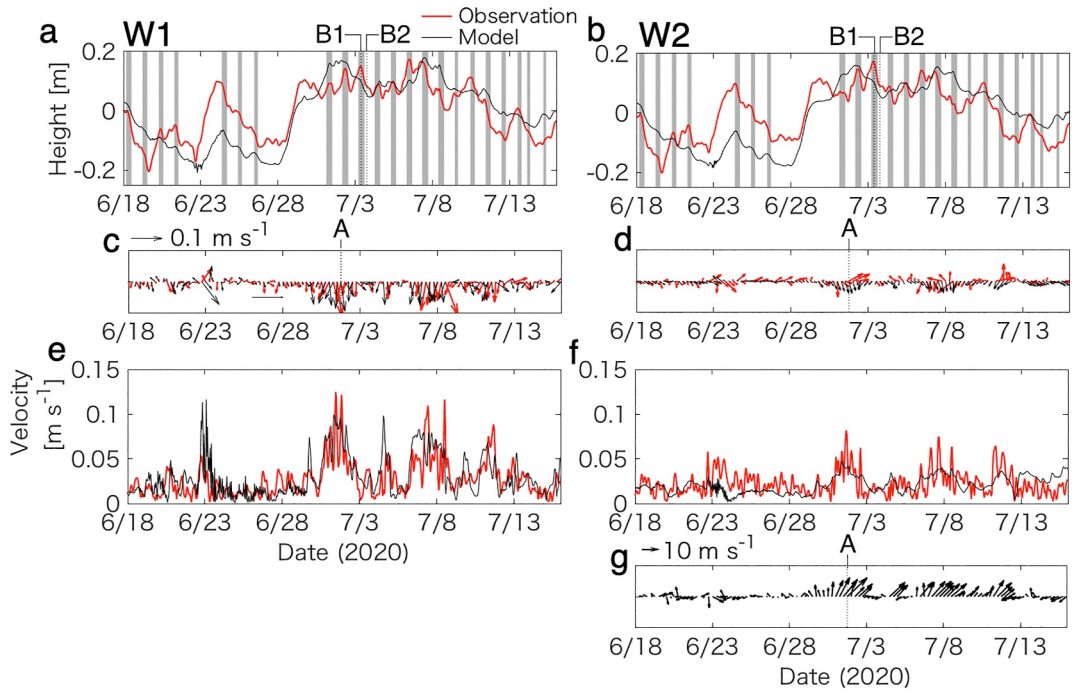

Figure 6. (a–f) Observed and modeled (a, b) surface height, (c, d) vertically averaged velocity vectors and (e, f) vertically averaged velocity magnitude at (a, c, e) Stn. W1 and (b, d, f) Stn. W2, and (g) wind forcing over the West Lake. Periods A, B1, and B2 are referenced in Figures 5 and 6.

periods at the river barrage). Effects of the water gates are clear in a comparison of sea-surface heights obtained at the ocean and lake sides near the river barrage (Figure 5d). When the water gates are opened, the surface height on the lake side follows the tidal elevations on the ocean side. On the other hand, when the gates are closed, the surface height in the lake is independent of the tidal elevations. Upstream/reverse (north-west ward) currents occur at Stn. N2 right after the water gates close. These upstream flows are associated with operations of the water gates that generate horizonal pressure gradients in the study area (described in the following section).

At Stn. W1 and W2 in West Lake, the modeled velocity magnitudes are consistent with the observations, although there are over/under estimations of the sea-surface height and an inconsistency in the current direction at W2 (Figure 6). This inconsistency in the current direction at W2 is caused by chaotic small-scale eddies in the middle basin of West Lake when the currents are strong (see details in the next section). A reverse flow opposite to the wind direction also appears at Stn. W1 like Stn. N1.

The correlation coefficients of the sea-surface height and the velocity magnitude, the root mean square error (RMSE) between modeled and observed velocity magnitudes and comparisons between the observations and the numerical simulations of time-averaged velocity magnitude are listed in Table 1. According to the correlation

Table 1
Comparisons Between Observed and Modeled Results at the Our Mooring Stations

Station	Correlation coefficient		RMSE	Time-averaged velocity magnitude		
	Surface height	Velocity magnitude	Velocity magnitude [m s^{-1}]	Observations [m s^{-1}]	Model [m s^{-1}]	Relative error
N1	0.90	0.75	3.1×10^{-2}	3.0×10^{-2}	3.2×10^{-2}	8%
N2	0.54	0.66	1.8×10^{-2}	4.9×10^{-2}	5.0×10^{-2}	2%
W1	0.77	0.62	1.6×10^{-2}	2.8×10^{-2}	3.0×10^{-2}	9%
W2	0.70	0.34	2.0×10^{-2}	2.3×10^{-2}	2.1×10^{-2}	−6%

Note. Velocity magnitude is the magnitude of vertically averaged velocity ($V = \sqrt{[u]^2 + [v]^2}$, [ ] is vertical averaging). The averaging period for the time-averaged velocity magnitude is from June 18 to 16 July 2020.

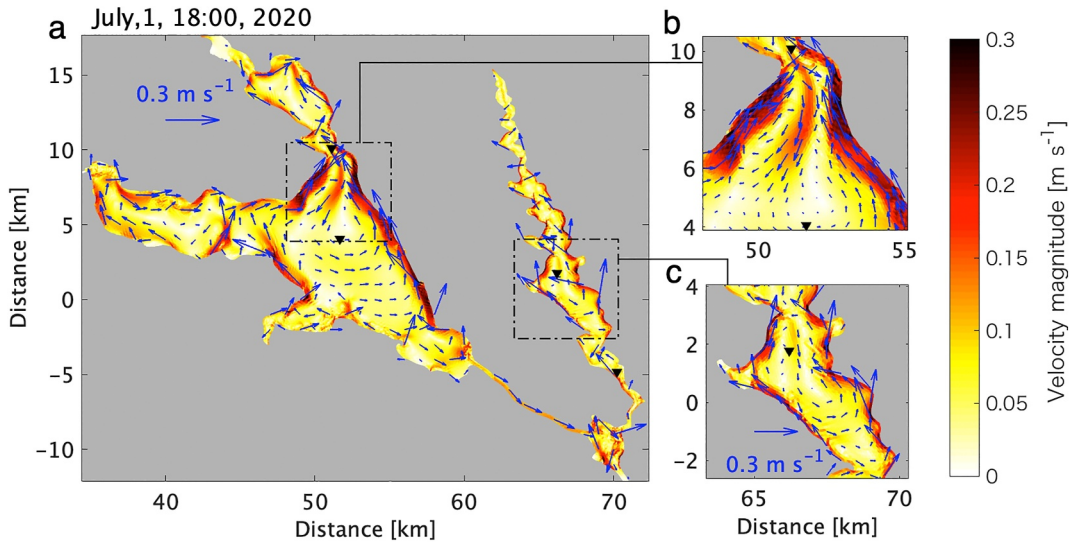

Figure 7. Surface velocity on July 1, 18:00, 2020 (period A shown in Figures 4 and 6) from the case with wind forcing. The black triangles indicate the locations of the ADCP observation sites.

coefficients, fluctuations of the surface height and velocity are accurately reproduced by the model except for the velocity magnitude at Stn. W2 and the sea-surface height at Stn. N2. The RMSE is $O(10^{-2})$ m s^{-1} (Table 1). The estimated errors are comparable to those of a previous model study in a lake (Valbuena et al., 2022). Differences in the time-averaged velocity magnitude are less than 9%, which indicates that the kinetic energy is similar between the observations and the model. Based on these results, we assume that the quality of the model is good enough to investigate water circulation and associated transport in the study area.

4. Results and Discussion

4.1. Water Circulation in the Lake System

The surface velocity distribution when the southerly wind blows is plotted in Figure 7 (1 July 2020 indicated as period A in Figures 4 and 6). The direction of currents is not consistent horizontally and appear to be greatly influenced by the topography of the lakes. Water is transported in the same direction as the wind along the coast, while reverse/counter flows occur in the middle of the channels (or example areas shown in Figures 7b and 7c). The counter (southward) flows in the middle of the channel are generated to conserve water masses that are transported to the north along the coast by the southerly wind. Generally, wind-driven counter flows at depth are driven by downwelling/upwelling at coastal boundaries in deep lakes (e.g., Bengtsson, 2012; Dargahi & Setegn, 2011; Lien & Hoopes, 1978). On the other hand, in shallow lakes with a large aspect ratio of the horizontal and vertical scales, wind forcing generate intensified flows along the coast and horizontal counter flows in the middle of lake basins (e.g., Curto et al., 2006; Podsetchine & Schernewski, 1999). Our study area, Lake Kasumigaura, is categorized as the latter type, which results in the middle channel counter flows.

Upstream flows appear at the end of North Lake, Stn. N2, right after the water gates close (Figure 5). Flow directions at both ends of West Lake and North Lake are in the downstream direction when the water gates open (Figure 8c, the timing of the snapshots is B1 indicated in Figure 5a). At this point in time, the pressure (surface height) increases as the distance increases at the location of the river barrage (water gates) (Figure 8a), viz., the pressure in North Lake is between West Lake and the river barrage. The pressure increases right after the water gates close around the downstream end, but the pressure gradient between West and North Lake persists due to a shallow and narrow river between them, which results in the upstream reverse flows in North Lake (Figures 8b and 8d, the timing of the snapshots is B2 indicated in Figure 5a). Periods of intensified upstream flows occur approximately 4–5 hr after the water gates close.

The kinetic energy is a useful quantity to evaluate lake dynamics associated with water circulations. In order to investigate water motions caused by external forcing, we estimated the kinetic energy defined as

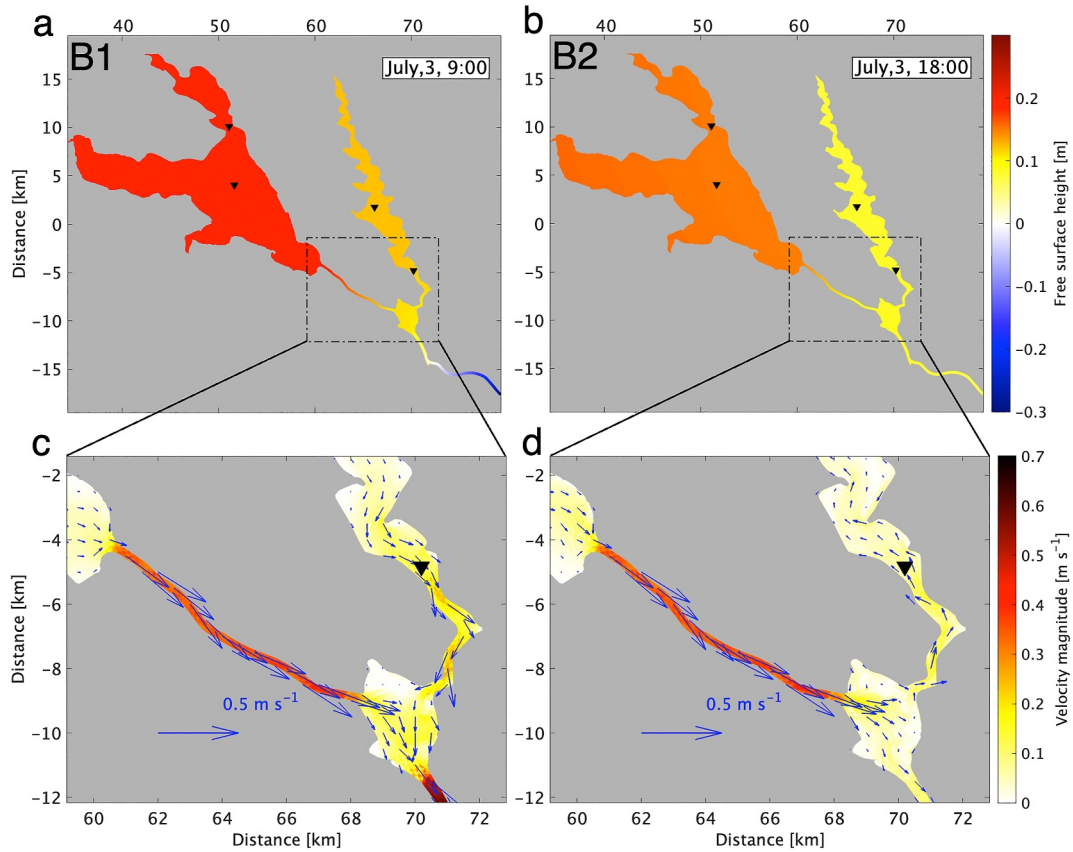

Figure 8. (a, b) Surface height and (c, d) surface velocity on July, 3, 9:00 and July 3, 18:00, 2020 (periods "B1" and "B2" shown in Figures 4–6, respectively). The black triangles indicate the locations of the ADCP observation sites.

$$E_K = \frac{1}{2}(u^2 + v^2 + w^2), \tag{6}$$

where u, v and w are the zonal, meridional and vertical currents, respectively. The time- and vertically averaged kinetic energy is enhanced along the coast and in the middle of the narrow channels (Figure 9a). The enhanced kinetic energy in the middle of the channels is due to wind-induced counter flows. The area-, monthly and vertically averaged E_K are compared between West Lake and North Lake and with wind stress (Figures 9c and 9e). The averaging/integration areas for the two lakes are indicated by regions surrounded by the chain-dotted black boxes in Figure 9a. Variations of E_K are consistent with the wind stress, τ_W, as indicated by the correlation coefficients between E_K and τ_W which are 0.90 and 0.95 for West Lake and North Lake, respectively (Figure 9e, $p << 0.01$). A difference between yearly averaged E_K for the two lakes is approximately 5%, thus the kinetic energy in the two lakes is essentially the same.

As shown in Figures 9b, 9d, and 9f, the magnitude of E_K without wind forcing is much lower in the lake basins than it is with wind forcing. The intensified E_K is confined to the rivers connecting West Lake and North Lake, and the vicinity of the river discharge points (Figure 9b). The yearly averaged E_K in North Lake is approximately 6 times higher than that in West Lake. This difference is caused by the narrow shape of North Lake and effects of the river barrage. The monthly averaged E_K can be explained by the weight of the river discharges, W_Q, as indicated by the correlation coefficients between E_K and W_Q which are 0.90 and 0.80 for West Lake and North Lake, respectively (Figures 9d and 9f, $p << 0.01$). E_K is higher in the early part of the year (January–July) than in the latter part of the year (Figure 9d). The high E_K is caused by high W_Q due to precipitation in January–July (see Figures 3a and 3b). The model case without wind forcing explains E_K only 3% and 17% of the total kinetic energy obtained from the model case with wind forcing for West Lake and North Lake, respectively. Therefore, wind forcing dominates the kinetic energy except in the narrow rivers connecting West Lake and North Lake.

10.1029/2024WR037509

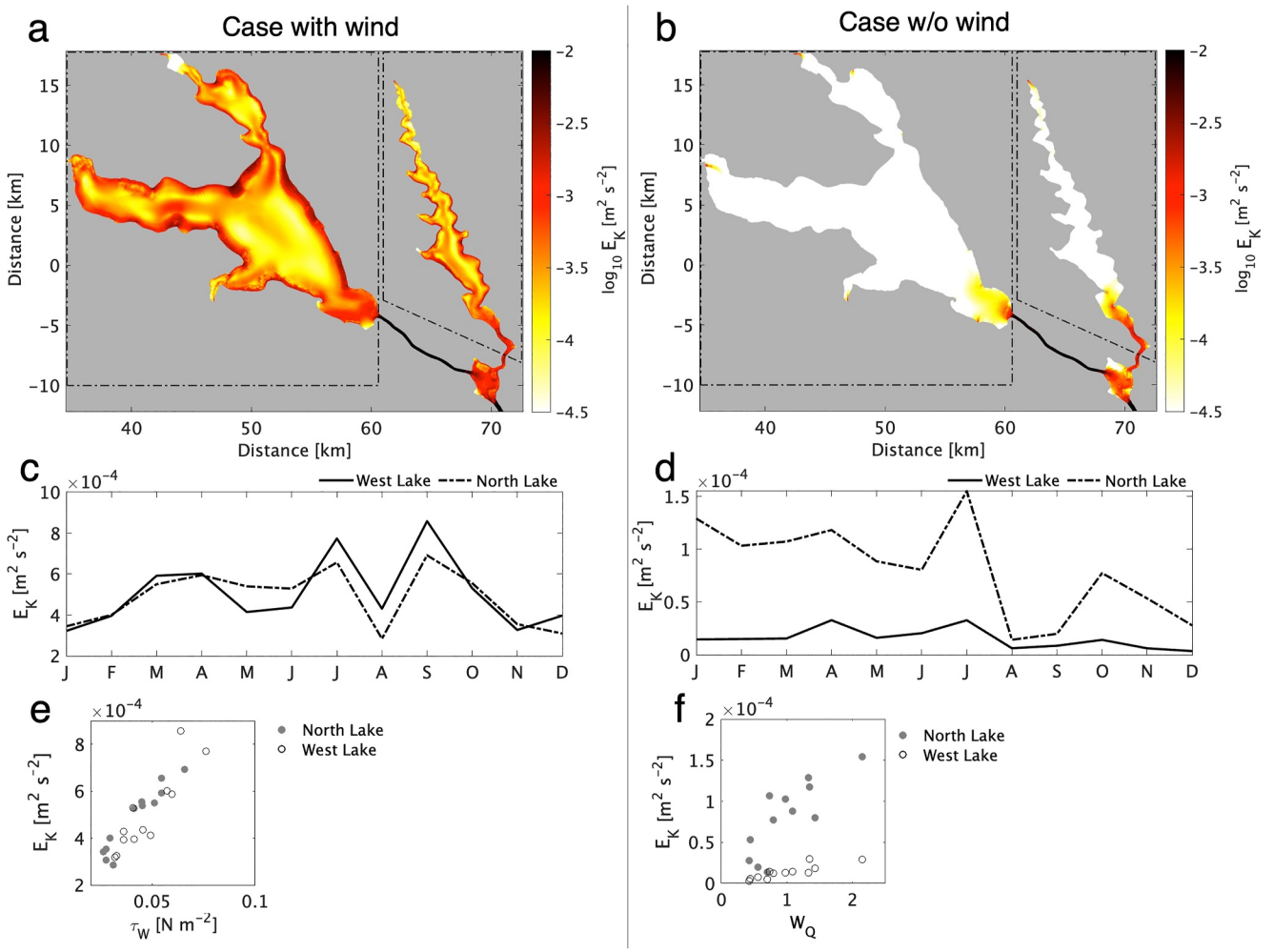

Figure 9. Model results of kinetic energy for the model cases (left) with wind forcing and (right) without wind forcing. Time and vertically averaged kinetic energy, (c, d) monthly and spatially averaged kinetic energy in the (solid line) West lake and (chain-dotted line) North Lake, (e) monthly averaged kinetic energy as a function of the monthly averaged wind stress (τ_W) and (f) monthly averaged kinetic energy as a function of the monthly averaged weight of river discharge (W_Q). Chain-dotted black boxes in panels (a, b) represent integration areas for spatial-averaging for the West Lake and North Lake.

4.2. Tracer Transport and Residence Time

Released passive tracers generate plume-like structures from rivers and gradually spread downstream over time (Figure 10). In the figure, white color ($C = 0$) and dark red color ($C = 1$) indicate released water from the river boundaries and initially distributed water, respectively. Black arrows in Figure 10a represent the four major river discharge points. Released water from the rivers is mixed with ambient water accompanied by eddy motions and filament-like structures. The tracer concentration gradually increases with increasing distance from the major river locations in the narrow channels in West Lake and North Lake. Meanwhile, in the middle basin of West Lake, tracers are mixed and a clear upstream-downstream variation does not appear. Tracers are not directly transported downstream due to mixing in the West Lake basin, which causes a higher tracer concentration in the West Lake basin than North Lake. The tracer concentration in the West Lake basin is approximately twice that in North Lake on days = 120–180 (Figures 10d–10f).

The model is forced by seasonal winds which are dominated by north and south winds in winter and summer, respectively (Figure 3d). A previous numerical study reported that wind direction relative to the coast line significantly influences tracer transport and residence time in a shallow bay (Razmi et al., 2014). Indeed, in our numerical model, horizontal circulation is strongly influenced by the wind direction as shown in Figures 5 and 6. The model run starts on 1 January 2020, and the flushing time scale, T_f, is approximately six month for

10.1029/2024WR037509

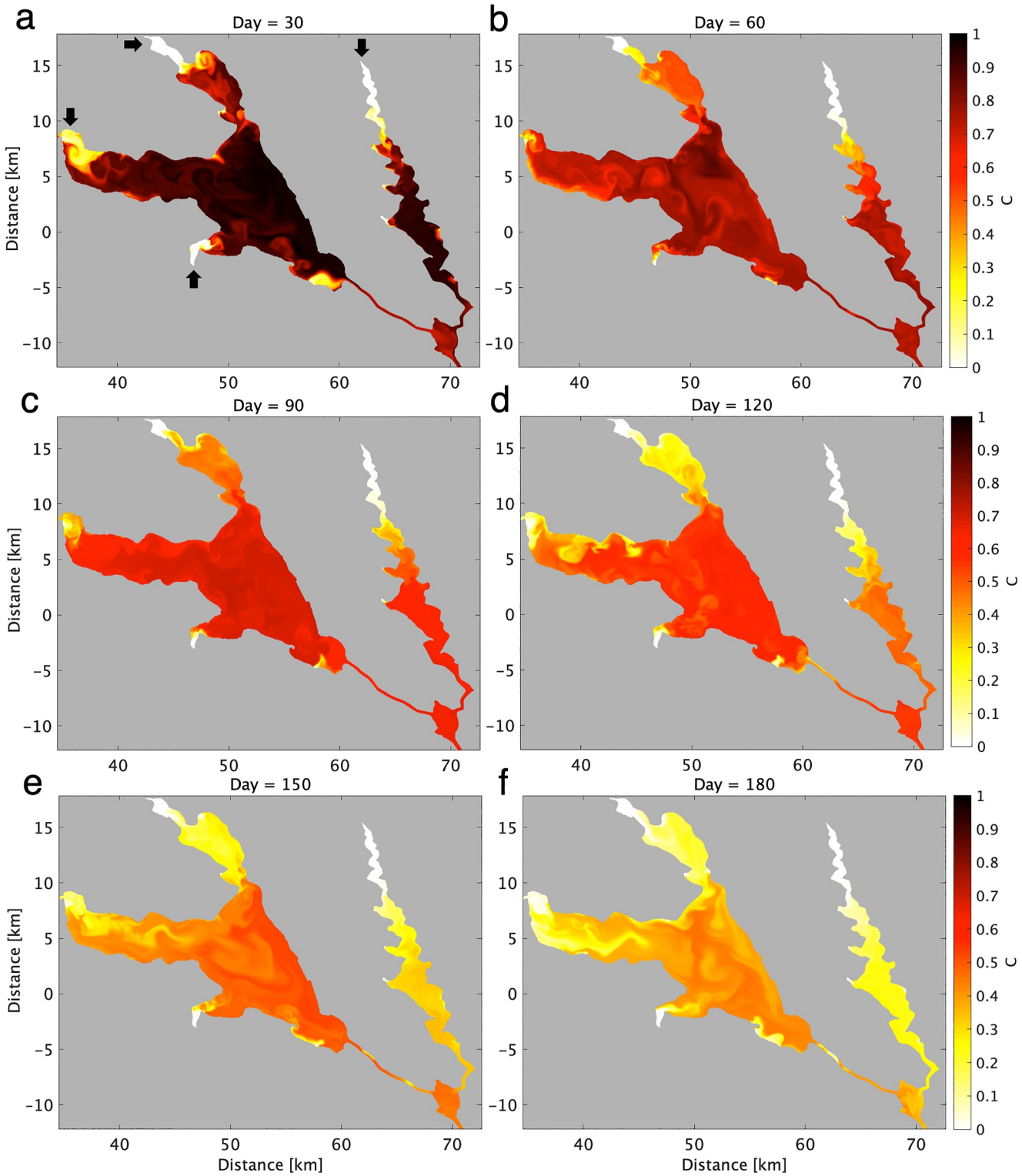

Figure 10. Distributions of the surface tracer concentration on days (a) 30, (b) 60, (c) 90, (d) 120, (e) 150, (f) 180 for the model case with wind forcing. Black arrows in panel (a) show locations of the major river discharges.

West Lake. The dominant north wind forcing in the beginning of the model run might influence the modeled tracer distribution.

The tracer distribution from the model case without wind forcing is significantly different from the case with wind forcing (Figure 11). Released tracers do not mix with ambient water and there are strong tracer gradients between the river and ambient waters. This implies that river water simply penetrates through ambient water downstream without wind forcing, viz., the situation seems to be close to the linear case represented as Equation 2 (Figure 1).

In order to evaluate the residence time of the water in the lakes, the e-folding decay time scale of the tracer concentration, T_e, is computed from the model outputs between 0 and 180 days (Figure 12). The residence time scale T_e is calculated by fitting $\exp(-t/T_e)$ to the modeled time series of tracer concentration at each grid point. For the model case with wind forcing, T_e gradually increases as with distance from the major river inputs in the narrow channel regions with T_e less than approximately 150 days (Figure 12a). T_e exceeds 200 days in the middle of West Lake basin (Figure 12a, x-distance $\sim$ 50–60 km, y-distance ~ -5 to 5 km). On the otherhand, the maximum T_e in North Lake is approximately 130 days. Therefore, the residence time of North Lake is generally shorter than that of West Lake. The e-folding decay time scale for the model case without wind forcing shows a similar pattern as the tracer concentration (Figure 12b). Extremely high values of T_e appear on the downstream end of West Lake because discharged river water does not reach these regions within 180 days (Figures 11f and 12b). The remaining highly concentrated tracer on the downstream end of West Lake is flushed away over time after 180 days (not shown). Except in the downstream of West Lake, T_e is much lower and is less than $\sim$100 days for the model case without wind forcing than that with wind forcing. According to the results above, the tracer distributions and residence times are signficantly influenced by wind-induced motions in the lakes.

4.3. Turbulent Mixing and Tracer Dispersion

The nondimensional relative vorticity, ξ/f, where $\xi = \partial v/dx - \partial u/\partial y$ is the relative vorticity and $f = 8.6 \times 10^{-5}$ s^{-1} is the inertial frequency, indicates enhanced eddy motions driven by vortex shedding due to flows along the rough shoreline (Figure 13a). The magnitude of the nondimensional relative vorticity is much higher than unity along the shore, thus eddy motions are not influenced by the earth's rotation. Intensified horizontal velocity shear also appears on the shore, which would lead to turbulent eddy motions (Figure 13b). High vorticity, shear and KE regions are confined to the coastal boundaries, which implies that intensified mixing is limited to those regions (Figures 9a and 13). However, mixed water is transported to the entirety of the lakes (Figures 10 and 12a). This mismatch can be explained as follows: (a) tracers from the rivers ($C = 0$) are released from the boundaries, (b) the released tracers ($C = 0$) and initial tracers ($C = 1$) are mixed due to intensified eddy and shear near the boundaries, and (c) mixed water ($0 < C < 1$) is transported to the lake basins by the large-scale circulation.

The Reynolds number, $Re = D\langle u_M \rangle/\nu$, is computed by the horizontal width scale, D, the time and spatially averaged velocity magnitude, u_M, and the horizontal eddy viscosity, $\nu = 0.1$ m^2 s^{-1}. Re, D, and u_M are shown in Table 2. The horizontal width scale is defined by the diameter of the largest circle surrounded by the coast, 7,400 m and 2,400 m for West Lake and North Lake, respectively (the largest circles are indicated by magenta circles in Figure 13a). The horizontal width scale is approximately 3 times larger for West Lake than for North Lake. The Reynolds number for both of West Lake and North Lake exceeds a typical critical Re, 300, leading to turbulent motions due to eddy shedding effects (e.g., Blevins, 1990). In addition, the velocity magnitudes occasionally exceed 0.1 m s^{-1} when strong wind blows (see Figure 7), in which case Re exceeds 7,400 and 2,400 for West Lake and North Lake, respectively. Although turbulent motions should not be simply evaluated with the Reynolds number for natural water system in which the earth's rotation and complicated topography are important (e.g., McWilliams, 2016), these results still imply stronger mixing would occur in the large West Lake rather than the narrow-shaped North Lake. On the other hand, for the model case without wind forcing, Re is much lower than the model case with wind forcing, and turbulent eddy motions are not expected to appear. Laminar flow in the model without wind forcing is also evident as indicated by the smooth tracer distribution shown in Figure 11. Therefore, chaotic eddy motions attributed to wind forcing mix lake water and lead to an increase in the residence time scale.

The domain-averaged tracer concentration represents the water flushing ratio between the ambient lake water ($C = 1$) and discharged river water ($C = 0$) in the study area. When the domain-averaged C is one or zero, water in the system is completely occupied by ambient water or discharged river water, respectively. The water flushing

10.1029/2024WR037509

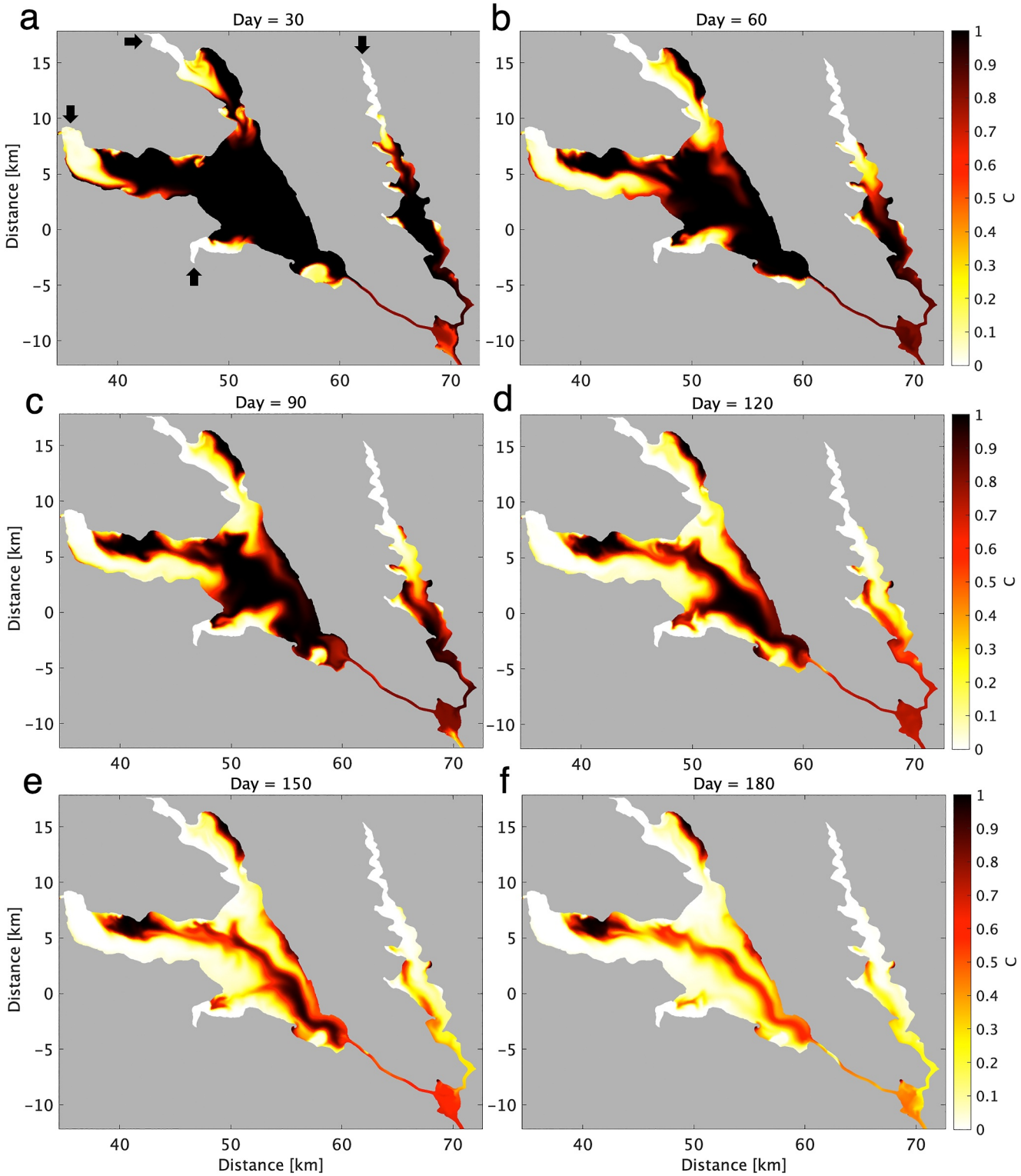

Figure 11. As in Figure 9, but for the model case without wind forcing.

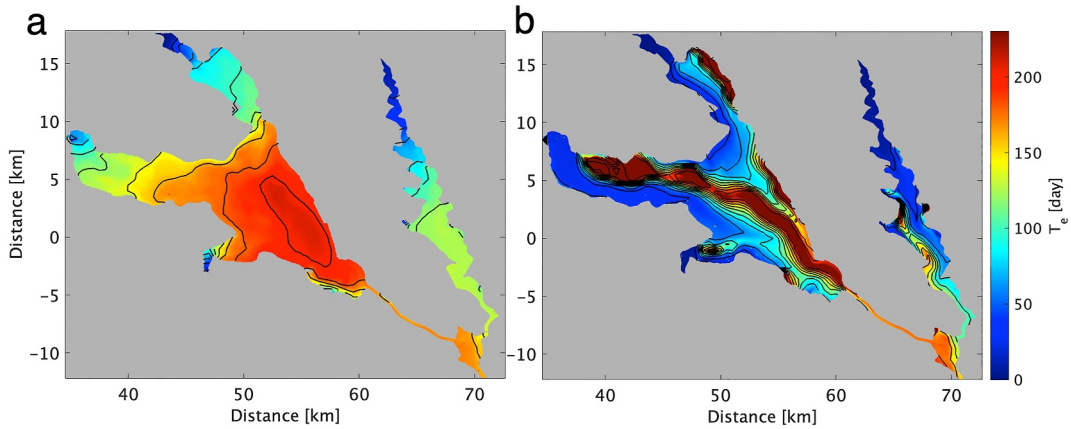

Figure 12. Maps of the e-folding tracer decay time scale, T_e, for the model cases (a) with and (b) without wind forcing. Black contours indicate T_e with an interval of 20 days.

ratio from model results is plotted in Figure 14 with theoretical solutions from the linear model (Equation 2) and the CSTR model (Equation 3). The theoretical solution of the linear model is computed with

$$C_{\text{linear}}(t) = C(0)\,\frac{V(t) - \int_o^t Q(t)\,dt}{V(t)}, \tag{7}$$

where $C(0)$ is the initial tracer concentration and the solution for the CSTR model is estimated numerically with

$$C_{\text{CSTR}}^{n+1} = \frac{C^n(V^n - Q^n\Delta t)}{V^n}, \tag{8}$$

where n indicates the time step and Δt is the time-step size, $\Delta t = t^{n+1} - t^n$. As mentioned in the introduction, the water flushing ratio ranges between the solutions from these two models and approaches the CSTR solution as mixing increases in a system. The water flushing ratio is closer to the CSTR solution for West Lake than that for North Lake. This difference is consistent with the residence time scale (Figure 12a) and the Reynolds number (Table 2). We define the mixing ratio, R_{mix}, based on the ratio between the CSTR solution and model results as follows

$$R_{\text{mix}} = \frac{C_{\text{CSTR}}}{C} \times 100 \tag{9}$$

where the factor of 100 produces a percentage, C_{CSTR} is the CSTR solution. The mixing ratio, R_{mix}, is calculated at the timing of the flushing time scale, $t = T_f$, defined by Equation 1. The flushing times are 182 and 145 days for

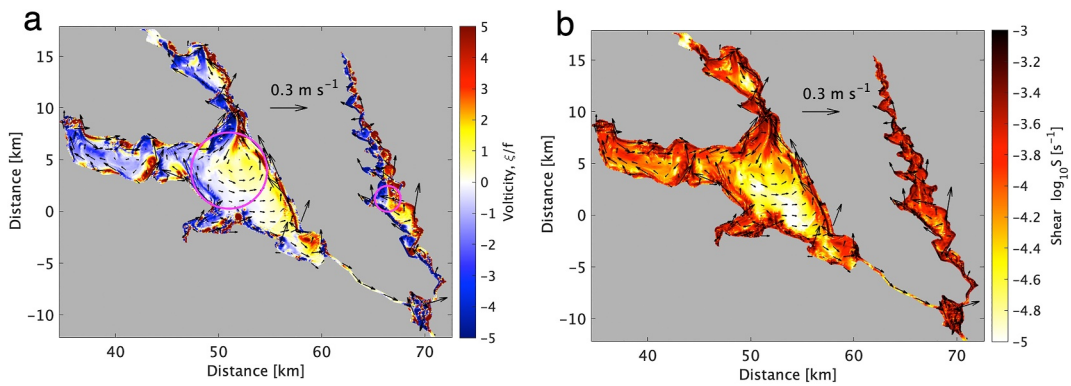

Figure 13. (a) Nondimensional relative vorticity, ξ/f, and (b) horizontal velocity shear on July 1, 18:00, 2020. Black vectors show surface velocity.

Table 2
Horizontal Width Scale (D), Time and Spatially Averaged Velocity Magnitude (u_M) and Reynolds Number (Re) for West and North Lake

	D [m]	$\langle \overline{u_M} \rangle$ [m s^{-1}]	Re
West Lake	7,400	2.2×10^{-2}	1,650
		(2.7×10^{-3})	(200)
North Lake	2,400	2.1×10^{-2}	511
		(5.0×10^{-3})	(120)

Note. Values in brackets are for the model case without wind forcing.

West Lake and North Lake, respectively. For the model case with wind forcing, R_{mix} are 89% and 72% for West Lake and North Lake, respectively. This difference is caused by intensified mixing in the wide shaped West Lake. R_{mix} values are much lower for the model cases without wind forcing than with wind forcing and are given by 57% and 37% for West Lake and North Lake, respectively. Despite the lack of eddying motions, the value of R_{mix} is still appreciable without wind forcing and is likely due to laminar shear-flow dispersion in the lakes (Fischer, 1979). In addition, because of very low velocities along the shoreline without wind forcing, tracers remain in these regions and lead to an increase in R_{mix} for the model case without wind forcing (see Figure 11).

It is well known that shear dispersion in natural flows is much greater than dispersion by molecular diffusion (Fischer, 1979) or numerical diffusion (e.g., Burchard & Rennau, 2008; Holleman et al., 2013). Thus, explicit horizontal scalar diffusion is not needed in the transport equation. According to shear dispersion summarized by Fischer et al. (1979), the diffusion coefficient in laminar flows caused by shear dispersion is given analytically by

$$K_{F79} = \frac{r^2 u_0^2}{192 K_{\mathrm{mol}}} \tag{10}$$

where r is the radius of the pipe/channel, u_0 is the velocity on the centerline and K_{mol} is the molecular diffusion. This formula indicates that shear dispersion increases as the horizontal scale, r or $D = 2r$, increases. Because the diffusion coefficient, K_{F79}, estimated from Equation 10 works only for laminar natural flows, it does not work for our study area that is influenced by turbulent eddy motions under high Reynolds numbers. Instead, we attempted to estimate the diffusion coefficient using the advection-diffusion formula as follows.

The advection-diffusion equation for the time- and cross-sectionally averaged tracer concentration $\langle \overline{C} \rangle$ along a channel is given by (Monismith et al., 2002)

$$\frac{\partial}{\partial x}\left(Q\langle \overline{C} \rangle\right) = \frac{\partial}{\partial x}\left(AK_C \frac{\partial \langle \overline{C} \rangle}{\partial x}\right), \tag{11}$$

where A is the cross-sectional area, $\langle \cdot \rangle$ is the time- and cross-sectional average, Q is the volumetric flow rate along the channel, x is the longitudinal distance along the channel, and K_C is the longitudinal dispersion coefficient. Integrating Equation 11 with respect to x and assuming $K_C = C = 0$ at $x = 0$ (the upstream end), K_C can be expressed as

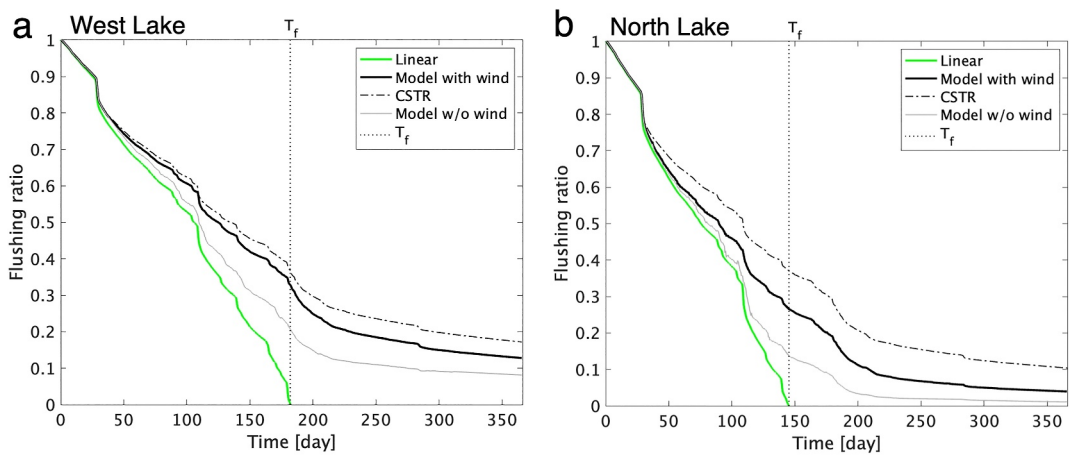

Figure 14. (a, b) Water flushing ratio computed from the model cases with wind forcing (black line) and without wind forcing (gray line), simple linear model (green line), and continuously stirred tank reactor model (chain-dotted black line) for (a) West Lake and (b) North Lake.

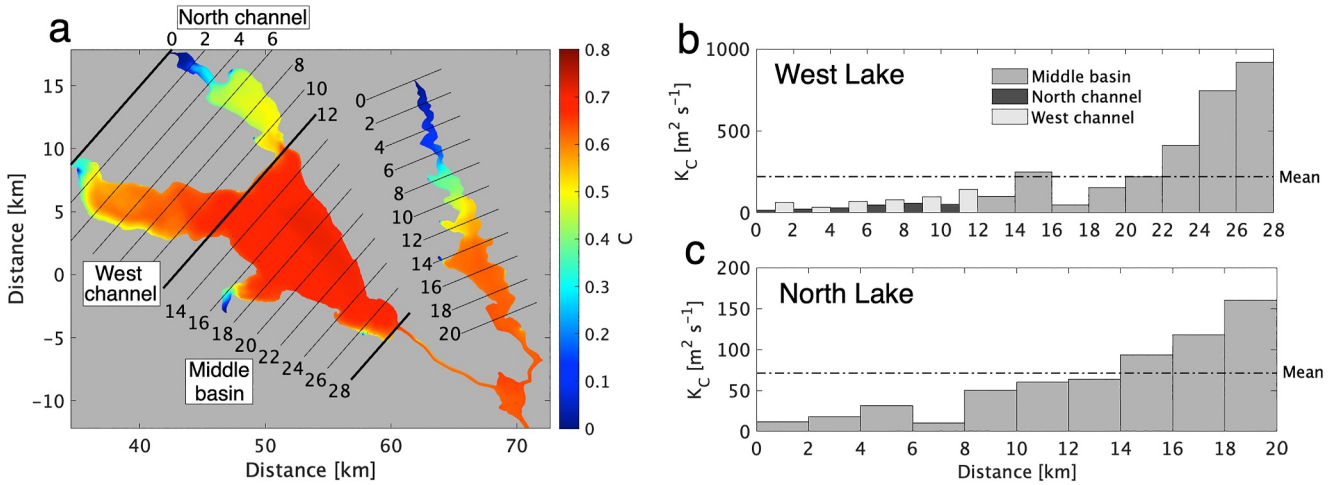

Figure 15. (a) Time-averaged tracer concentration as a function of downstream distance in West Lake and North Lake, and (b, c) horizontal dispersion computed in 2 km bins for (b) West Lake and (c) North Lake. The horizontal dispersion in the upstream part of West Lake is separated into the north channel (dark gray) and the west channel (light gray). Note that the vertical axis range is different for (b) and (c).

$$K_C = \frac{Q\langle\overline{C}\rangle}{A\partial\langle\overline{C}\rangle/\partial x} = \frac{\overline{u}_{\text{down}}\langle\overline{C}\rangle}{\partial\langle\overline{C}\rangle/\partial x} \tag{12}$$

Where $\overline{u}_{\text{down}} = Q/A$ the time- and cross-sectionally averaged downstream velocity. Using this formula, the domain-averaged K_C (integrating from the up-to downstream ends of both lakes) are given by 229 m^2 s^{-1} and 72 m^2 s^{-1} for West Lake and North Lake, respectively. The ratio between the two is approximately three which is consistent with the fact that the dispersion coefficient scales with a product of a length scale and a velocity scale DU, and the velocity scale U is roughly the same for both lakes while the width scale, D (Table 2), is roughly three times larger in West Lake. The numerical diffusion coefficient can be estimated with (Burchard & Rennau, 2008).

$$K_{\text{num}} = \frac{1}{2}u\Delta x\left(1 - \frac{u\Delta t}{\Delta x}\right). \tag{13}$$

Based on the averaged velocity show in Table 2 of 2.2×10^{-2} m s^{-1}, a horizontal grid spacing of 100 m and a time step size of 10 s, the numerical diffusion is 1.1 m^2 s^{-1}, which is two orders of magnitude smaller than the longitudinal dispersion coefficient.

The longitudinal dispersion coefficient, K_C, is estimated within 2 km bins for West and North Lakes from the upstream boundaries (Figure 15). West Lake is separated into three sub domains, the middle basin (distance >12 km) and two upstream narrow channels (north and west channels, distance <12 km), for the K_C calculations (Figure 15a). The dispersion generally increases with downstream distance x except for some small-scale variations. The enhanced diffusivity on the downstream ends of the lakes is due to water gate-induced flows intensified in the narrow downstream channels (see Figures 5, 8c, and 8d). The domain averaged dispersion coefficient in the four region is shown in Table 3. The estimated dispersion coefficient in the middle of West Lake basin is much higher than other regions, which is due to the wide nature of the basin that allows for the creation of larger-scale structures that more efficiently mix the tracer.

We define the Péclet number (Jenkins, 2003) in the lakes as

$$\text{Pe} = \frac{\overline{u_{\text{down}}}L}{K_C}, \tag{14}$$

where L is the length of the sub-domains (Figure 15a and Table 3). Advective (dispersive) transport dominates when Pe >> 1 (<<1). The Péclet number is an important parameter to understand transport processes in water systems and oceans (e.g., Jenkins, 2003; Luo et al., 2021). Luo et al. (2021) evaluated the residence time scale in

Table 3
The Domain-Averaged Longitudinal Dispersion Coefficient, K_C, the Along Channel Length, L, the Flushing Time Scale, T_f, the Péclet Number, P_E, the Residence Time Scale of T_e and the Ratio of the Residence Time Scale to the Flushing Time Scale, T_e/T_f

		K_C [m^2 s^{-1}]	L [km]	T_f [days]	P_E	T_e	T_e/T_f
West Lake	Total	229	28	182	0.43	159	0.87
	Middle basin	371	16	–	0.17	186	1.02
	North channel	34	12	–	1.14	90	0.49
	West channel	86	12	–	0.44	138	0.76
North Lake		72	20	145	1.13	99	0.68

an enclosed bay based on the order of Pe ∼10 and concluded that the residence time scale is dominated by advection processes in their study area. Estimated Pe values in the two lakes and sub-domains are listed in Table 3. The Péclet number is approximately unity in North Lake, viz., both of advection and dispersive processed are equally important for tracer transport. For West Lake, Pe varies in the sub-domains between 0.17 and 1.14. Dispersive transport dominates in the middle basin where Pe = 0.17. On the other hand, Pe is approximately unity for the narrow-shaped north channel in West Lake, which is similar to the narrow North Lake. These results imply that the shape of the lakes dictates the relative importance of advection versus dispersion.

The Péclet number is compared to the nondimensional residence time (T_e/T_f) in Figure 16 and Table 3. We expect this nondimensional residence time to be unity under the CSTR condition. We used T_f estimated from the total area of West Lake for computing the nondimensional residence time for the three sub-domains in West Lake. The ratio of T_e/T_f is slightly higher than unity, 1.02, for the middle basin in West Lake, which is likely caused by tracer left in the middle of the lake basin (see Figure 12a, x ∼ 50–60 km, y ∼ 0–5 km). The comparison of Pe and T_e/T_f shows an inverse relationship between them indicating that the residence time increases with an increase in mixing as indicated by a decrease in Pe. According to our model results, $T_e/T_f \sim 1$ when Pe ∼ 0.1 and $T_e/T_f \sim 1/2$ when Pe ∼ 1.

4.4. Earth's Rotational Effects

The Rossby number quantifies the relative influence of the earth's rotation and is given by

$$R_O = \frac{U}{L_F f}, \tag{15}$$

where U is the velocity magnitude and L_F is length scale of interest. The earth's rotation strongly influences circulation when $R_O < 1$. If U and L_F are assumed to be $O(0.1)$ m s^{-1} and $O(10^3)$ m (1 km), respectively, $R_O = O(1)$, indicating that the earth's rotation moderately influence water circulation. The e-folding tracer decay time scale, T_e, from the model cases without Coriolis forcing is shown in Figure 17. For the case with wind forcing, T_e is nearly identical to that from the model with Coriolis forcing (compare Figures 12a and 17a). Other results, such as residence time and dispersion coefficient, are nearly the same for the model cases with and without Coriolis forcing (not shown). On the other hand, for the model cases without wind forcing, model results show clear effects of the earth's rotation on the tracer distributions (compare Figures 12b and 17b). For the case with Coriolis forcing, tracers from the river mouths tend to be transported along the coast to their right (Figure 12b), which is a typical feature of the earth's rotational effects in the northern hemisphere.

We explain two possible reasons for the small/negligible Coriolis effects on our realistic forcing case with wind forcing: (a) locally enhanced eddy motions not bounded by the Coriolis forcing and (b) unsteady wind forcing. First,

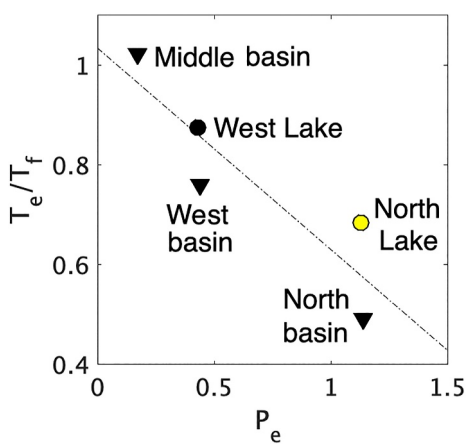

Figure 16. Nondimensional residence time scale, T_e/T_f, as a function of the Péclet number, Pe. A dot-dashed line indicates a linear regression between Pe and T_e/T_f computed with the least squares method.

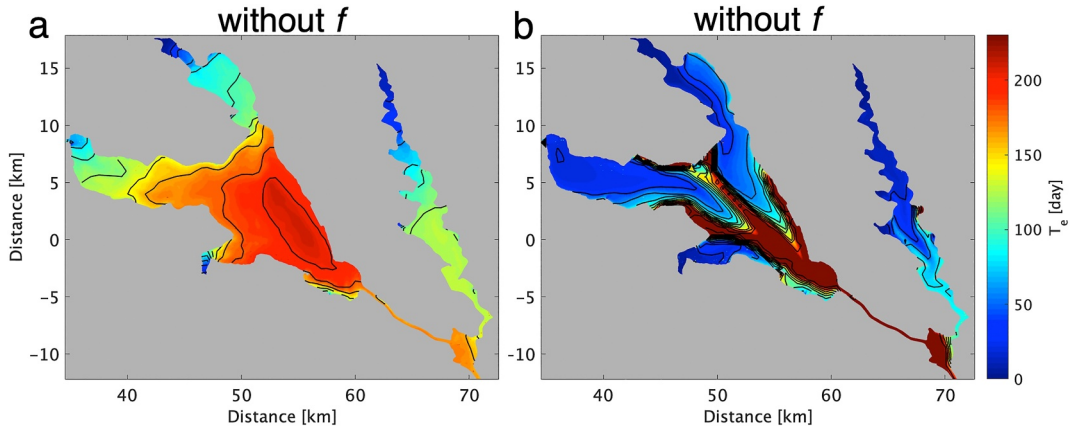

Figure 17. Same as Figure 12, but for the model cases without the Coriolis forcing.

the estimated Rossby number, $R_O \sim 1$, may not be representative of all relevant motions in the lake system. Small-scale eddy motions are locally enhanced by wind forcing with the velocity magnitude exceeding 0.3 m s^{-1} and would be locally enhanced in small regions less than 1 km (Figure 13). Under such a condition, $R_O > 1$, the earth's rotation does not significantly influence the dynamics. Indeed, the nondimensional relative vorticity reaches five in intensified eddy motions along the coast (Figure 13a). Eddy motions in such high-vorticity regions are not influenced by the earth's rotation. In addition, Amadori et al. (2020) reported that the Rossby number is not a suitable parameter for Ekman currents in enclosed basins.

The second reason for the weak effect of Coriolis forcing is the unsteady wind forcing. Developments of Ekman transport require steady winds with a time scale longer than the inertial period $2\pi f^{-1}$, which is 20.3 hr at our study site. The wind direction and speed fluctuate and change over time scales of a few hours, or much shorter than the inertial period (Figures 3c and 3d). These high-frequency fluctuations in the wind forcing are caused by land-sea breezes owing to differential heating on land areas around the study site and in the adjacent Pacific Ocean (Masunaga et al., 2023). Wind-induced Ekman transport does not have time to develop under highly unsteady wind forcing. For these reasons, the earth's rotation does not significantly influence the wind-induced circulation at our study site.

5. Conclusions

This study investigated water circulation processes and residence time scales in the Lake Kasumigaura system, Japan, using a high-resolution numerical model, SUNTANS. The lake system consists of a large lake, West Lake, and narrow-shaped lake, North Lake, and connected channels. Model results were compared with field observations and showed good agreement. Kinetic energy induced by the wind stress was much higher than that due to river discharges, and thus wind-induced currents dominated in the lake system except in narrow channels. The flow speed in the narrow channels was intensified by operations of water gates located at the downstream end of the lake system. The model domain was initially occupied with a tracer concentration of unity and water from river discharges/boundaries were set to zero, which allows us to evaluate water exchange processes and mixing between lake and river water. The model is simplified without stratification and without heat flux, but we assume that the model is able to provide reasonable tracer transport because time scales of vertical mixing are much shorter than the residence time scale.

Water from the river discharges partially mixed with lake water owing to wind-induced motions. Mixing appeared to be stronger in the large lake, West Lake, than in the narrow-shaped North Lake. This difference in the mixing can be explained by differences in the horizontal length scales of the lakes. The length scale is approximately three times higher in West Lake than in North Lake. The domain-averaged tracer concentration was between the CSTR and the no-mixing linear limits calculated with Equations 2 and 3. The residence time scale is closer to the CSTR condition in West Lake owing to the intensified mixing that is higher than in North Lake. The estimated longitudinal dispersion coefficient, K_C, was estimated as 229 m^2 s^{-1} and 72 m^2 s^{-1} for

West Lake and North Lake, respectively. This dispersion coefficient varied in sub-domains in West Lake from its largest value of 371 $m^2\ s^{-1}$ in the middle basin to the smallest value of 34 $m^2\ s^{-1}$ in the narrow north channel. The Péclet number which characterizes the relative importance of advection versus diffusion was in the range 0.14–1.14 and was closely related to the normalized residence time scale, T_e/T_f, where T_e is the residence time scale based on the e-folding time scale and T_f is flushing time scale. Effects of the longitudinal dispersion on transport and residence times were directly controlled by the length scales in different regions of the lakes which were dictated by the shape of the shorelines. Earth's rotational effects do not significantly influence wind-induced water circulation and tracer transport at our study site.

As explained by the simple theories given by Equations 2 and 3 (Figure 1), water exchange processes in an enclosed domain are largely influenced by mixing conditions. However, residence time scales and water exchange processes have not been thoroughly investigated in the literature while considering the importance of horizontal diffusion and dispersion effects. This study employed numerical simulations for two medium size lakes and found that the shape and size of lakes significantly influenced dispersion processes and residence time scales. The results provide new insights into water exchange processes and residence time scales in lakes, reservoirs and similar enclosed water systems.

Appendix A: River Discharges

This appendix presents detailed information for the river discharge forcing used in the model. The annually averaged river discharge, Q_M, is derived from observed river discharge data at 32 river months shown in a report by Ibaraki Prefecture (Maeda, 2012). Several river mouths are merged into one discharge points, when those are located closely. Finally, we set 20 river discharge points in the numerical domain (Figure A1): 10 for West Lake (No. 1–10), nine for North Lake (No. 12–20) and one for the connected river between the two lakes (No. 11). The report from Ibaraki Prefecture also presents the residual water discharge which is defined by the difference between observed river discharges and estimated total river discharge from precipitation in the catchment area. The residual river discharge represents river discharges from uncountable numerous rivers into the lakes. The residual river discharge is 5.54 and 2.71 $m^3\ s^{-1}$ for West Lake and North Lake, respectively, and is equally added to the modeled river discharges. The final values of the river discharge used for the all river months are summarized in Table A1.

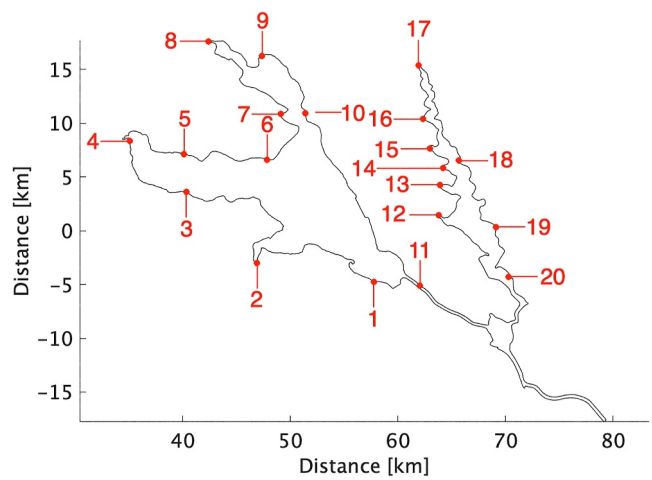

Figure A1. Locations of the 20 river discharge points with the numbers corresponding to those Table A1.

Table A1
The Annually Averaged River Discharge, Q_M, Used for the River Discharge Boundaries

No.	1	2	3	4	5	6	7	8	9	10
Q_M [m^3 s^{-1}]	5.60	5.20	1.00	12.68	0.34	1.26	0.97	6.88	3.68	1.75
No.	11	12	13	14	15	16	17	18	19	20
Q_M [m^3 s^{-1}]	4.33	0.91	0.64	0.32	0.77	0.76	6.24	0.52	0.91	0.75

Note. The numbers in this table correspond to those in Figure A1.

Appendix B: Vertical Distributions of Velocity Profiles

Comparisons of vertical distributions of the ADCP-derived currents and those from the SUNTANS model are presented in this Appendix. Modeled velocities show similar intensified flow patterns to observed data from the ADCP when the wind speed is strong at Stn. N1 in North Lake, especially for the zonal component (Figure B1, date ~ June 23, July 2 and July 8). However, when the wind is weak, observed velocity shows high-frequency noisy motions that do not appear in the model. Due to the high-frequency fluctuations in the observed data, modeled velocities do not agree with the observed ADCP velocity data in each bin. For example, the correlation coefficient between modeled and observed velocity magnitude at the bin closest to the surface is 0.21 for Stn. N1. The observed high-frequency motions may be caused by noise related to the acoustic observations or sub-grid scale turbulent motions not resolved by the Reynolds averaged numerical model. In addition, obvious vertical variability in the flow patterns are not evident in the observations, which is probably due to the shallow depth of the study site. At Stn. N2 located in a shallow channel at the south end of North Lake, observed velocity structures are essentially uniform in the vertical (Figures B2a and B2c). Comparisons of vertical velocity distributions in West Lake (Stn. W1 and W2) from the ADCP observations and the SUNTANS model are shown in Figures B3 and B4. Similar to the observed velocity at Stn N1 in North Lake, observed velocity in West lake also shows high-frequency noisy motions, which are absent in the model results. For these reasons, vertically averaged velocities are used for model validation in this study.

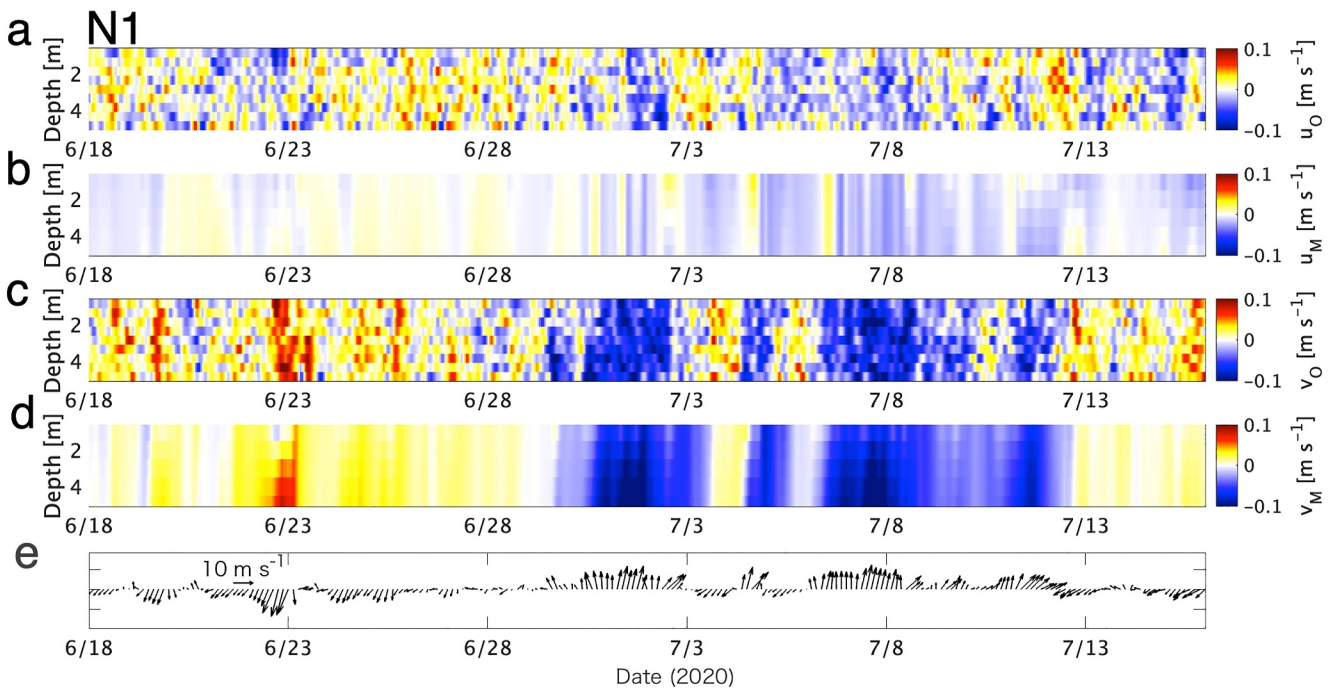

Figure B1. (a, c) Observed and (b, d) modeled vertical flow structures, and (e) wind forcing at Stn. N1. Panels (a, b) and (c, d) represents meridional and zonal flow components, respectively.

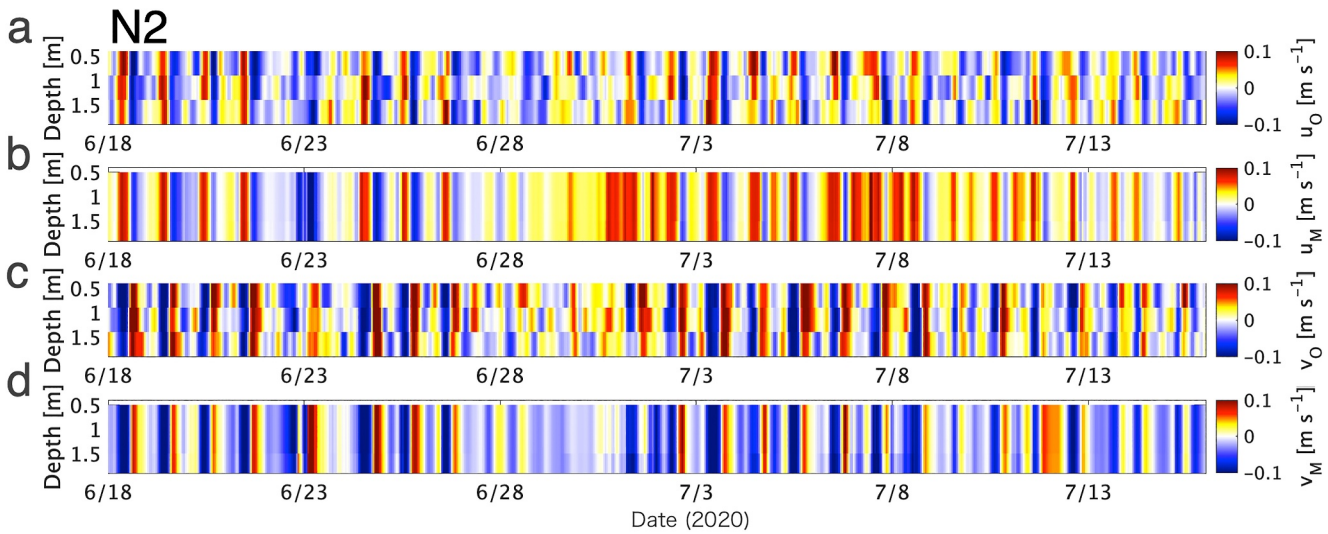

Figure B2. Same as Figure B1, but for Stn. N2.

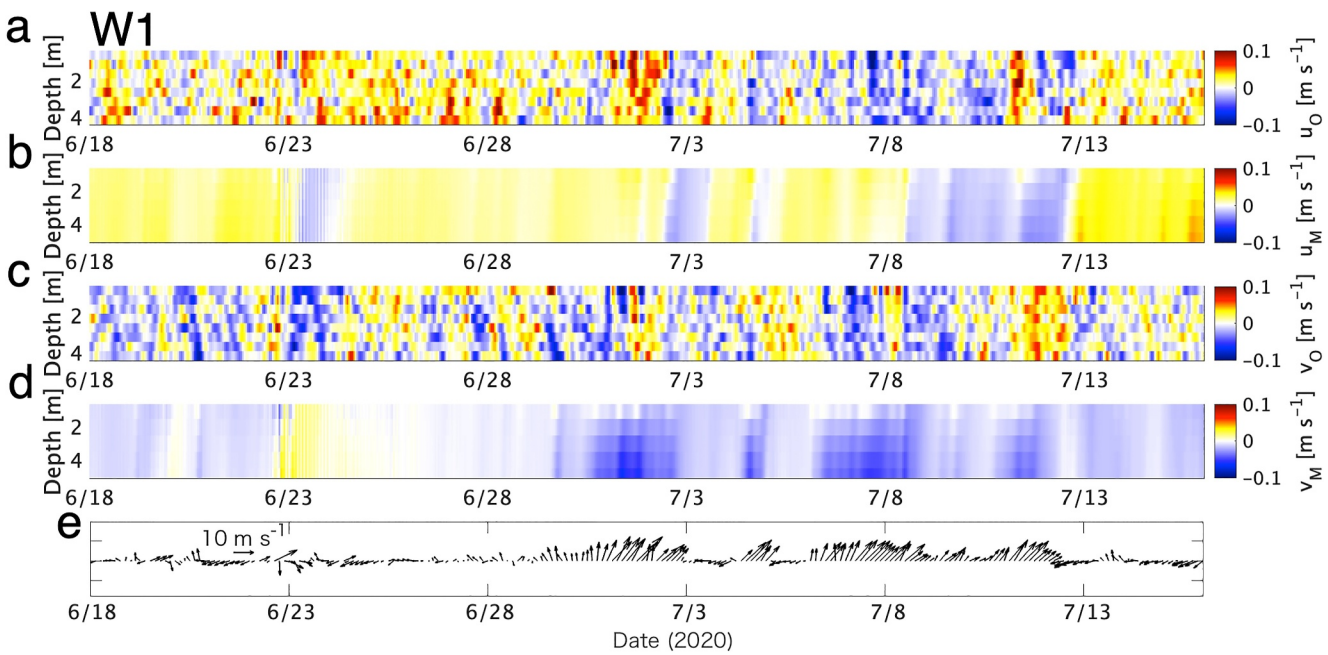

Figure B3. Same as Figure B1, but for Stn. W1.

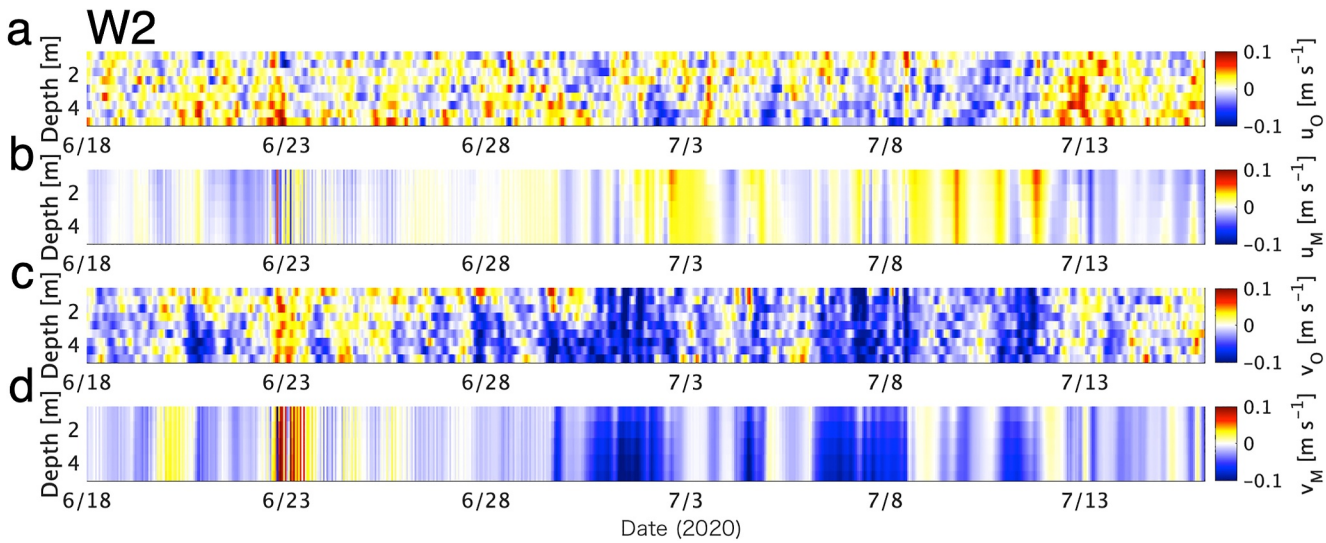

Figure B4. Same as Figure B1, but for Stn. W2.

Data Availability Statement

The numerical model used in this study is available at repository of figshare with all source codes and input files (Masunaga, 2024a). ADCP measurement data used for the model validations is available at Masunaga (2024b). Our model data set is able to be used for scientific research purposes other than commercial purposes by clearly indicating the reference.

Acknowledgments
This study was supported by the Japan Society for the Promotion of Science Grant-in-Aid for Scientific Research (22K18018 and 22H05201) and the S-18-3 project founded by the Environmental Restoration and Conservation Agency of Japan (Grant JPMEERF20S11811).

References

Amadori, M., Piccolroaz, S., Dijkstra, H. A., & Toffolon, M. (2020). What makes an elongated lake 'large'? Scales from wind-driven steady circulation on a rotating Earth. *Journal of Great Lakes Research*, *46*(4), 703–717. https://doi.org/10.1016/j.jglr.2019.10.013

Ambrosetti, W., Barbanti, L., & Sala, N. (2003). Residence time and physical processes in lakes. *Journal of Limnology*, *62*(1s), 1–15. https://doi.org/10.4081/jlimnol.2003.s1.1

Auger, G. A., Kelly, M. R., Moriarty, V. W., Rose, K. C., & Kolar, H. R. (2024). Understanding lake residence time across spatial and temporal scales: A modeling analysis of Lake George, New York USA. *Water Resources Research*, *60*(2), e2022WR034168. https://doi.org/10.1029/2022wr034168

Bengtsson, L. (2012). Circulation processes in lakes. In *Encyclopedia of lakes and reservoirs* (pp. 162–165). Springer.

Blevins, R. D. (1990). *Flow-induced vibration* (2nd ed.). Van Nostrand Reinhold.

Burchard, H., & Rennau, H. (2008). Comparative quantification of physically and numerically induced mixing in ocean models. *Ocean Modelling*, *20*(3), 293–311. https://doi.org/10.1016/j.ocemod.2007.10.003

Busu, B. K., & Pick, F. R. (1996). Factors regulating phytoplankton and zooplankton biomass in temperate rivers. *Limnology & Oceanography*, *41*(7), 1572–1577. https://doi.org/10.4319/lo.1996.41.7.1572

Casulli, V., & Zanolli, P. (2005). High resolution methods for multidimensional advection–diffusion problems in free-surface hydrodynamics. *Ocean Modelling*, *10*(1–2), 137–151. https://doi.org/10.1016/j.ocemod.2004.06.007

Choi, J., Troy, C., Hawley, N., McCormick, M., & Wells, M. (2020). Lateral dispersion of dye and drifters in the center of a very large lake. *Limnology & Oceanography*, *65*(2), 336–348. https://doi.org/10.1002/lno.11302

Curto, G., Józsa, J., Napoli, E., Krámer, T., & Lipari, G. (2006). Large scale circulations in shallow lakes. Advances in fluid mechanics. *Vorticity and turbulence effects in fluid structure interactions*, *45*, 83–104.

Dargahi, B., & Setegn, S. G. (2011). Combined 3D hydrodynamic and watershed modelling of Lake Tana, Ethiopia. *Journal of Hydrology*, *398*(1–2), 44–64. https://doi.org/10.1016/j.jhydrol.2010.12.009

da Silva, D. V., Oleinik, P. H., Costi, J., de Paula Kirinus, E., & Marques, W. C. (2019). Residence time patterns of Mirim Lagoon (Brazil) derived from two-dimensional hydrodynamic simulations. *Environmental Earth Sciences*, *78*(5), 1–11. https://doi.org/10.1007/s12665-019-8162-y

Eshleman, K. N., & Hemond, H. F. (1988). Alkalinity and major ion budgets for a Massachusetts reservoir and watershed 1. *Limnology & Oceanography*, *33*(2), 174–185. https://doi.org/10.4319/lo.1988.33.2.0174

Fischer, H. B. (1979). *Mixing in inland and coastal waters*. Academic Press.

Fischer, H. B., List, J. E., Koh, C. R., Imberger, J., & Brooks, N. H. (1979). *Mixing in inland and coastal waters*. Academic Press.

Fringer, O. B., Dawson, C. N., He, R., Ralston, D. K., & Zhang, Y. J. (2019). The future of coastal and estuarine modeling: Findings from a workshop. *Ocean Modelling*, *143*, 101458. https://doi.org/10.1016/j.ocemod.2019.101458

Fringer, O. B., Gerritsen, M., & Street, R. L. (2006). An unstructured-grid, finite-volume, nonhydrostatic, parallel coastal ocean simulator. *Ocean Modelling*, *14*(3–4), 139–173. https://doi.org/10.1016/j.ocemod.2006.03.006

Grimes, D. J., Feddersen, F., Giddings, S. N., & Pawlak, G. (2020). Cross-shore deformation of a surfzone-released dye plume by an internal tide on the inner shelf. *Journal of Physical Oceanography*, *50*(1), 35–54. https://doi.org/10.1175/jpo-d-19-0046.1

Holleman, R., Fringer, O., & Stacey, M. (2013). Numerical diffusion for flow-aligned unstructured grids with application to estuarine modeling. *International Journal for Numerical Methods in Fluids*, *72*(11), 1117–1145. https://doi.org/10.1002/fld.3774

Homma, T., Komatsu, N., Negishi, M., Nakamura, K., & Park, H. D. (2008). Relationship between Microcystis morphospecies composition and nutrient concentration in the water basin (Nishiura, Kitaura) of Kasumigaura, Japan. *Nippon Suisan Gakkaishi*, *74*(2), 189–198. https://doi.org/10.2331/suisan.74.189

Ito, W., Nakayama, K., & Shintani, T. (2023). Coriolis effects on wind-driven upwelling in enclosed basins. *Continental Shelf Research*, *256*, 104956. https://doi.org/10.1016/j.csr.2023.104956

Jenkins, W. J. (2003). Tracers of ocean mixing. In *The oceans and marine geochemistry* (pp. 223–246).

Kratzer, C. R., & Biagtan, R. N. (1997). Determination of travel times in the lower San Joaquin River basin, California, from dye-tracer studies during 1994-1995. *US Department of the Interior, US Geological Survey*, *97*(4018).

Li, Y., Acharya, K., & Yu, Z. (2011). Modeling impacts of Yangtze River water transfer on water ages in Lake Taihu, China. *Ecological Engineering*, *37*(2), 325–334. https://doi.org/10.1016/j.ecoleng.2010.11.024

Lien, S. L., & Hoopes, J. A. (1978). Wind-driven, steady flows in Lake Superior 1. *Limnology & Oceanography*, *23*(1), 91–103. https://doi.org/10.4319/lo.1978.23.1.0091

Lucas, L. V., Cloern, J. E., Thompson, J. K., & Monsen, N. E. (2002). Functional variability of habitats within the Sacramento–San Joaquin Delta: Restoration implications. *Ecological Applications*, *12*(5), 1528–1547. https://doi.org/10.2307/3099989

Luo, C., Lin, L., Shi, J., Liu, Z., Cai, Z., Guo, X., & Gao, H. (2021). Seasonal variations in the water residence time in the Bohai Sea using 3D hydrodynamic model study and the adjoint method. *Ocean Dynamics*, *71*(2), 157–173. https://doi.org/10.1007/s10236-020-01438-5

Maeda, O. (2012). *An introduction to Kahology* (Vol. II-4). Ibaraki Prefecture.

Masunaga, E. (2024a). Lake Kasumigaura circulation model 2020 [dataset]. https://doi.org/10.6084/m9.figshare.26411125

Masunaga, E. (2024b). ADCP observation data in Lake Kasumigaura in summer 2020 [dataset]. https://eiji.eng.ibaraki.ac.jp/WRR_2024/

Masunaga, E., Itoh, S., & Kitamura, T. (2023). Vertical mixing and oxygen flux caused by daily sea breezes in a shallow stratified lake. *Limnology*, *24*(2), 95–109. https://doi.org/10.1007/s10201-022-00707-0

McWilliams, J. C. (2016). Submesoscale currents in the ocean. *Proceedings of the Royal Society A: Mathematical, Physical and Engineering Sciences*, *472*(2189), 20160117. https://doi.org/10.1098/rspa.2016.0117

Monismith, S. G., Kimmerer, W., Burau, J. R., & Stacey, M. T. (2002). Structure and flow-induced variability of the subtidal salinity field in northern San Francisco Bay. *Journal of Physical Oceanography*, *32*(11), 3003–3019. https://doi.org/10.1175/1520-0485(2002)032<3003:safivo>2.0.co;2

Monsen, N. E., Cloern, J. E., Lucas, L. V., & Monismith, S. G. (2002). A comment on the use of flushing time, residence time, and age as transport time scales. *Limnology & Oceanography*, *47*(5), 1545–1553. https://doi.org/10.4319/lo.2002.47.5.1545

Morillo, S., Imberger, J., & Antenucci, J. (2006). Modifying the residence time and dilution capacity of a reservoir by altering internal flow-paths. *International Journal of River Basin Management*, *4*(4), 255–271. https://doi.org/10.1080/15715124.2006.9635295

Nakamura, K., & Aizaki, M. (2016). Effect of suspended solid on light attenuation in the shallow and turbid Lake Kasumigaura, Japan. *Japanese Journal of Limnology*, *77*(1), 13–23. https://doi.org/10.3739/rikusui.77.13

Okubo, A. (1971). Oceanic diffusion diagrams. *Deep-Sea Research*, *18*(8), 789–802. https://doi.org/10.1016/0011-7471(71)90046-5

Peeters, F., & Hofmann, H. (2015). Length-scale dependence of horizontal dispersion in the surface water of lakes. *Limnology & Oceanography*, *60*(6), 1917–1934. https://doi.org/10.1002/lno.10141

Podsetchine, V., & Schernewski, G. (1999). The influence of spatial wind inhomogeneity on flow patterns in a small lake. *Water Research*, *33*(15), 3348–3356. https://doi.org/10.1016/s0043-1354(99)00035-4

Rayson, M. D., Gross, E. S., Hetland, R. D., & Fringer, O. B. (2016). Time scales in Galveston Bay: An unsteady estuary. *Journal of Geophysical Research: Oceans*, *121*(4), 2268–2285. https://doi.org/10.1002/2015jc011181

Razmi, A. M., Barry, D. A., Lemmin, U., Bonvin, F., Kohn, T., & Bakhtyar, R. (2014). Direct effects of dominant winds on residence and travel times in the wide and open lacustrine embayment: Vidy Bay (Lake Geneva, Switzerland). *Aquatic Sciences*, *76*(S1), 59–71. https://doi.org/10.1007/s00027-013-0321-8

Romo, S., Soria, J., Fernández, F., Ouahid, Y., & Barón-Solá, Á. N. G. E. L. (2013). Water residence time and the dynamics of toxic cyanobacteria. *Freshwater Biology*, *58*(3), 513–522. https://doi.org/10.1111/j.1365-2427.2012.02734.x

Rueda, F., Moreno-Ostos, E., & Armengol, J. (2006). The residence time of river water in reservoirs. *Ecological Modelling*, *191*(2), 260–274. https://doi.org/10.1016/j.ecolmodel.2005.04.030

Stevens, C. L., Lawrence, G. A., & Hamblin, P. F. (2004). Horizontal dispersion in the surface layer of a long narrow lake. *Journal of Environmental Engineering and Science*, *3*(5), 413–417. https://doi.org/10.1139/s04-035

Stocker, R., & Imberger, J. (2003). Horizontal transport and dispersion in the surface layer of a medium-sized lake. *Limnology & Oceanography*, *48*(3), 971–982. https://doi.org/10.4319/lo.2003.48.3.0971

Valbuena, S. A., Bombardelli, F. A., Cortés, A., Largier, J. L., Roberts, D. C., Forrest, A. L., & Schladow, S. G. (2022). 3D flow structures during upwelling events in lakes of moderate size. *Water Resources Research*, *58*(3), e2021WR030666. https://doi.org/10.1029/2021wr030666

Vitousek, S., & Fringer, O. B. (2011). Physical vs. numerical dispersion in nonhydrostatic ocean modeling. *Ocean Modelling*, *40*(1), 72–86. https://doi.org/10.1016/j.ocemod.2011.07.002

Vollenweider, R. A. (1976). Advances in defining critical loading levels for phosphorus in lake eutrophication. *Mem Ist Ital Idrobiol*, *33*, 53–83.